Available online at www.sciencedirect.com
ScienceDirect
Journal of Computational Physics 227 (2008) 5105–5143
JOURNAL OF COMPUTATIONAL PHYSICS
www.elsevier.com/locate/jcp

Three-dimensional boundary conditions for direct and large-eddy simulation of compressible viscous flows

Guido Lodato *, Pascale Domingo, Luc Vervisch

INSA – Rouen, UMR-CNRS-6614-CORIA, Campus du Madrillet, Avenue de l'Université, BP 8, 76801 Saint Etienne du Rouvray Cedex, France

Received 24 September 2007; received in revised form 18 January 2008; accepted 22 January 2008
Available online 7 February 2008

Abstract

Navier–Stokes characteristic boundary conditions (NSCBC) usually assume the flow to be normal to the boundary plane. In this paper, NSCBC is extended to account for convection and pressure gradients in boundary planes, resulting in a 3D-NSCBC approach. The introduction of these additional transverse terms requires a specific treatment for the computational domain's edges and corners, as well as a suited set of compatibility conditions for boundaries joining regions associated to different flow properties, as inlet, outlet or wall. A systematic strategy for dealing with edges and corners is derived and compatibility conditions for inlet/outlet and wall/outlet boundaries are proposed. Direct numerical simulation (DNS) tests are carried out on simplified flow configurations at first. 3D-NSCBC brings a drastic reduction of flow distortion and numerical reflection, even in regions of strong transverse convection; the accuracy and convergence rate toward target values of flow quantities is also improved. Then, 3D-NSCBC is used for large-eddy simulation (LES) of a free jet and an impinging round-jet. Edge and corner boundary treatment, combining multidirectional characteristics and compatibility conditions, yields stable and accurate solutions even with mixed boundaries characterized by bad posedness issues (e.g. inlet/outlet). LES confirms the effectiveness of the proposed boundary treatment in reproducing mean flow velocity and turbulent fluctuations up to the computational domain limits.

Keywords: Non-reflecting boundary conditions; Compressible flows; Direct numerical simulation; Large-eddy simulations

1. Introduction

The treatment of boundary conditions is one of the most recurrent issues in computational fluid dynamics. Compressible solvers' accuracy, in general, is strongly sensitive to boundary solution, which may be spoiled by spurious numerical reflections generated at open boundaries. This motivates the necessity for strategies to reduce reflection and set up transparent boundary conditions.

* Corresponding author.
E-mail addresses: guido.lodato@coria.fr, guido.lodato@gmail.com (G. Lodato), pascale.domingo@coria.fr (P. Domingo), luc.vervisch@coria.fr (L. Vervisch).

0021-9991/$ - see front matter © 2008 Elsevier Inc. All rights reserved.
doi:10.1016/j.jcp.2008.01.038

The boundary conditions provide a way to anticipate the flow behavior at the very limit of the computational domain. The flow properties at the boundaries must derive from the knowledge of the inside of the computational domain, coupled with some approximations of the outside flow features. Departures between inside and boundary flows add numerical noise to the solutions. High-order numerical schemes widely used in direct numerical simulation (DNS) and large-eddy simulation (LES), do not dissipate the spurious modes that may be generated at the boundaries; the boundary conditions must therefore be designed so that physically correct solutions are produced, while minimizing the amplitude of any extraneous perturbation added to the flow.

The situation gets even more complicated when dealing with turbulent flows, where an excess of numerical reflection at open boundaries can significantly affect important physical flow properties, such as vorticity. As opposed to Reynolds-averaged Navier–Stokes computations (RANS), in LES a wide range of length and time scales is resolved and transported by the flow; the open boundaries are therefore, invested with a complex set of sound and entropy waves and convected vorticity. Any excess in numerical reflection can lead to the buildup of spurious oscillations, which, being superposed to the computed solution, negatively affect the physical properties of the flow itself.

Several approaches have been proposed to tackle boundary conditions. Many of them are oriented toward the definition of transparent frontiers for computational aero-acoustics (CAA), where the high standards in this regard, make the task particularly challenging (see [19,9,6,2] for review and applications). Among them, techniques based on characteristics waves have motivated much attention. Initially developed for hyperbolic systems of Euler equations, these approaches decompose the flow in terms of characteristic waves traveling in the direction normal to the boundary, thus reducing the boundary problem to a suitable imposition of the incoming waves. The identification of incoming waves allows, in principle, a direct control over boundary reflection, as the boundary condition can be designed to prevent incoming perturbations [21,22] or to damp their amplitude while allowing smooth transients [15]. An extension to the Navier–Stokes equations has been thoroughly discussed by Poinsot and Lele [12], who have developed a systematic approach to account for viscous terms, known as Navier–Stokes characteristic boundary conditions (NSCBC). The method has been extended to multicomponent reactive flows [1,11] with different choices of primitive variables along with the inclusion of chemical source terms at the domain's frontiers [17]. Polifke et al. [13] proposed a reduction of the reflection coefficient for low-frequency normal incident waves, using a "plane masking" approach for the linear relaxation term. A low Mach number expansion has been discussed by Prosser [14], in order to decouple convective and acoustic effects, thus allowing non-reflective conditions for the acoustic length scales.

These methods mostly rely on the assumption that the flow at the boundary can be regarded as locally one-dimensional, aligned with the normal to the boundary. The incoming waves are therefore computed resorting to the so-called LODI system, which directly derives from the Navier–Stokes equations written for primitive variables in characteristic form. The terms involving derivatives in the directions defining the local boundary plane (convection, pressure gradient and viscous fluxes) are then computed from the interior of the computational domain, but without any specific coupling with the boundary treatment. In the following, these in-plane directions are called 'transverse directions' and the related terms are called 'transverse terms'. The single-dimensionality assumption, combined with transverse terms computed from the known interior, has proven to perform well when the flow is almost aligned orthogonally to the boundary. Nevertheless, flow distortion and high reflection appear when the flow crosses the boundary along different directions. The role played by the transverse terms in these distortions has been carefully identified by Yoo et al. [24], who proposed a modification to the NSCBC approach for two-dimensional turbulent counterflow flames. They show that an appropriate treatment of the transverse terms in the computation of incoming waves improves the accuracy and convergence rate toward target values for selected relaxed quantities, while reducing flow distortion even in regions characterized by strong transverse convection.

When transverse effects are included in three-dimensional computation of incoming waves, the problem arises on how to enforce proper boundary conditions on the edges and the corners of the computational domain. As discussed by Valorani and Favini [23], transverse terms on edges and corners are coupled with characteristic waves traveling along directions orthogonal to adjacent boundaries. Therefore, three-dimensional characteristic coupled waves must be considered. Furthermore, when different types of boundary conditions have to be enforced, it is in general necessary to prescribe compatibility conditions for those boundary conditions whose well-posedness is not inherently ensured (e.g. inlet/outlet boundary conditions where veloc-

ity, temperature and pressure are simultaneously imposed). Not much on this regard can be found in literature and the formulation of boundary conditions for edges and corners remains a feature somehow related to each specific problem.

The objective of this paper is threefold. First the NSCBC improvement proposed by Yoo et al. [24], who included transverse terms in the boundary analysis, is extended to three-dimensional flows. A systematic procedure to deal with three-dimensional computational domain's edges and corners is then proposed. Finally, compatibility conditions for inlet/outlet and wall/outlet nodes are presented. The resulting 3D-NSCBC approach is tested on simplified configurations. LES results of a turbulent free jet and a turbulent impinging round-jet are also reported. For the sake of clarity, all the details of the three-dimensional characteristic formulation leading to the explicit derivation of the equations for the edges and corners solution are recalled in Appendix A.

2. Governing equations

The dynamics of compressible viscous flow is described by the Navier–Stokes equations, which impose the conservation of mass, momentum and energy within the fluid element. In the present case, the system is augmented with an additional transport equation for a passive scalar Z (diffusing according to the Fick law), which carries informations on turbulent scalar mixing. In cartesian coordinates (with the Einstein summation convention) the system of equations reads

$$\frac{\partial \rho}{\partial t} + \frac{\partial}{\partial x_i}(m_i) = 0, \tag{1}$$

$$\frac{\partial m_i}{\partial t} + \frac{\partial}{\partial x_j}(m_i u_j) + \frac{\partial p}{\partial x_i} = \frac{\partial \tau_{ij}}{\partial x_j} \quad (i = 1, 2, 3), \tag{2}$$

$$\frac{\partial \rho E}{\partial t} + \frac{\partial}{\partial x_i}[(\rho E + p)u_i] = \frac{\partial}{\partial x_i}(u_j \tau_{ij}) - \frac{\partial q_i}{\partial x_i}, \tag{3}$$

$$\frac{\partial \rho Z}{\partial t} + \frac{\partial}{\partial x_i}(\rho Z u_i) = \frac{\partial}{\partial x_i}\left(\rho D \frac{\partial Z}{\partial x_i}\right), \tag{4}$$

where ρ is the fluid mass density, p is the thermodynamic pressure, $m_i = \rho u_i$ is the momentum density along the direction x_i and ρE is the total energy density (kinetic + thermal); under the assumption that the fluid is Newtonian and described by the ideal single-component gas law, the above system is closed by the following relations:

$$\frac{p}{\rho} = \mathcal{R} T, \tag{5}$$

$$\rho E = \frac{1}{2}\rho u_k u_k + \frac{p}{\gamma - 1}, \tag{6}$$

$$A_{ij} = \frac{1}{2}\left(\frac{\partial u_i}{\partial x_j} + \frac{\partial u_j}{\partial x_i}\right) - \frac{1}{3}\delta_{ij}\frac{\partial u_k}{\partial x_k}, \tag{7}$$

$$\tau_{ij} = 2\mu A_{ij}. \tag{8}$$

Here, T is the absolute temperature, $\mathcal{R}$ is the gas constant $\mathcal{R}^*/M_w$, where $\mathcal{R}^* = 8.32\ \mathrm{J/(mol\ K)}$ and M_w is the gas molar weight; $\gamma = c_p/c_v$ is the ratio between specific heat capacities at constant pressure and constant volume, which, in the present case, are expressed as

$$c_v = \frac{\mathcal{R}}{\gamma - 1}, \tag{9}$$

$$c_p = c_v + \mathcal{R}. \tag{10}$$

The dynamic viscosity of the fluid μ is expressed by the Sutherland's law:

$$\mu(T) = \mu_{\mathrm{ref}}\left(\frac{T}{T_{\mathrm{ref}}}\right)^{3/2}\frac{T_{\mathrm{ref}} + S}{T + S}. \tag{11}$$

Finally, the heat flux along x_i, namely q_i, is described by the Fourier law, while the thermal conductivity λ and the diffusion coefficient D are expressed from the dynamic viscosity, the Prandtl and Schmidt numbers:

$$q_i = -\lambda \frac{\partial T}{\partial x_i}, \quad \lambda = \frac{\mu c_p}{Pr}, \quad D = \frac{\mu}{\rho Sc} \tag{12}$$

(see Table 2 for a summary of the parameters' values used for the test-cases presented in the present paper).

3. Three-dimensional NSCBC

In NSCBC [12] the Navier–Stokes equations are written in their characteristic form to make explicit their dependency on the acoustic waves traveling across the boundary. Characteristic waves are represented by their amplitude time variations $\mathcal{L}_i$, $\mathcal{M}_i$ and $\mathcal{N}_i$, corresponding to the three physical-space directions (see Appendix A for details). The waves propagate in such a way that some of them leave the domain, while the others enter from outside. Incoming waves must be specified to close the boundary problem, as the outgoing ones can be computed from interior points and one-sided differences by directly applying their definition (Eqs. (A.16), (A.26) and (A.37)). The NSCBC approach prescribes that all the incoming wave amplitudes are imposed under the hypothesis that the flow at the boundary can be regarded as locally one-dimensional and inviscid. The resulting LODI system (A.20) is used to translate physical boundary conditions, expressed in terms of time derivatives of the primitive variables, into analytical relations involving the wave amplitude variations, such that the unknown incoming ones can be computed [12]. Once all the wave amplitudes are known, balance equations are used to advance the solution in time ((A.17) or (A.18) if the solver integrates the equations in conservative form).

When the flow is strongly three-dimensional at boundaries, the LODI assumption becomes too restrictive to keep boundary reflection at an acceptable level and nonphysical flow distortions appear, especially in regions where the flow is not aligned with the direction normal to the boundary. Furthermore, the pressure and any other relaxed quantity cannot reach the relevant physical target value in regions where strong convection in the boundary plane exists. Improved results are obtained by including in the computation of incoming wave amplitudes the transverse terms, namely convection and pressure gradients developing in the boundary plane [24].

Away from edges and corners of the computational domain, transverse terms can be evaluated from the computed solution using interior points. This direct approach, indeed, does not pose additional issues for inlet boundaries but, as already mentioned by Yoo et al. [24], can lead to serious numerical instabilities at outflow boundaries. One effective remedy for this is to add a small relaxation toward a reference value for the transverse terms, thus introducing a transverse damping coefficient β. As it will be shown when presenting results from selected test-cases, an expression can be proposed to relate β to flow properties and dynamically adjust this additional parameter.

At edges and corners of three-dimensional simulations a specific treatment is, however, needed. At these locations, transverse terms in a given boundary plane relate to characteristic waves traveling along directions that are orthogonal to adjacent boundary planes. The corresponding characteristic waves become coupled, leading to the need for a 3D-NSCBC approach.

The boundary treatment is first discussed for nodes away from edges and corners, then a specific method is proposed for edges and corners. In all the developments below, well-posedness of boundary conditions for Navier–Stokes equations is ensured following the approach used by Poinsot and Lele [12]: inviscid relations, corresponding to Euler boundary conditions, are first obtained and the correct number of boundary conditions for the Navier–Stokes equations is then achieved supplying additional viscous conditions. For each boundary type, the modification proposed in the present paper does not affect viscous conditions, which are then identical to those used by Poinsot and Lele.

3.1. Face boundaries

The solution at a face boundary is advanced in time using the Navier–Stokes equations (A.17) or (A.18). These equations have been written in terms of wave amplitudes $\mathcal{L}_i$.

For a boundary that is orthogonal to x_1, the $\mathcal{L}_i$ are obtained from their relations with time derivative of primitive variables, which are given by the system including transverse terms (in plane pressure gradient and convection) obtained from Eq. (A.17) by neglecting the viscous and diffusive terms $\boldsymbol{D}$ only:

$$\begin{cases} \frac{\partial \rho}{\partial t} + \frac{1}{c^2}\left[\mathcal{L}_2 + \frac{1}{2}(\mathcal{L}_5 + \mathcal{L}_1)\right] - \mathcal{T}_1 = 0, \\ \frac{\partial u_1}{\partial t} + \frac{1}{2\rho c}(\mathcal{L}_5 - \mathcal{L}_1) - \mathcal{T}_2 = 0, \\ \frac{\partial u_2}{\partial t} + \mathcal{L}_3 - \mathcal{T}_3 = 0, \\ \frac{\partial u_3}{\partial t} + \mathcal{L}_4 - \mathcal{T}_4 = 0, \\ \frac{\partial p}{\partial t} + \frac{1}{2}(\mathcal{L}_5 + \mathcal{L}_1) - \mathcal{T}_5 = 0, \\ \frac{\partial Z}{\partial t} + \mathcal{L}_6 - \mathcal{T}_6 = 0 \end{cases} \tag{13}$$

with the transverse contribution:

$$\boldsymbol{\mathcal{T}} = \begin{pmatrix} -\frac{\partial m_t}{\partial x_t} \\ -u_t \frac{\partial u_1}{\partial x_t} \\ -u_t \frac{\partial u_2}{\partial x_t} - \frac{1}{\rho}\frac{\partial p}{\partial x_2} \\ -u_t \frac{\partial u_3}{\partial x_t} - \frac{1}{\rho}\frac{\partial p}{\partial x_3} \\ -u_t \frac{\partial p}{\partial x_t} - \gamma p \frac{\partial u_t}{\partial x_t} \\ -u_t \frac{\partial Z}{\partial x_t} \end{pmatrix} \quad (t = 2, 3). \tag{14}$$

An alternative definition of $\boldsymbol{\mathcal{T}}$, using transverse fluxes computed on conservative variables, is given in Appendix B. The waves $\mathcal{L}_i$ are determined from this system, once physical boundary conditions are provided to approximate $\partial\rho/\partial t$, $\partial\mathbf{u}/\partial t$, $\partial p/\partial t$, $\partial Z/\partial t$. These physical boundary conditions are now discussed on the basis of Eq. (13) reorganized in terms of characteristic variables:

$$\begin{cases} \left(\frac{\partial p}{\partial t} - \rho c \frac{\partial u_1}{\partial t}\right) + \mathcal{L}_1 - \mathbb{T}_1^1 = 0, \\ \left(c^2 \frac{\partial \rho}{\partial t} - \frac{\partial p}{\partial t}\right) + \mathcal{L}_2 - \mathbb{T}_1^2 = 0, \\ \frac{\partial u_2}{\partial t} + \mathcal{L}_3 - \mathbb{T}_1^3 = 0, \\ \frac{\partial u_3}{\partial t} + \mathcal{L}_4 - \mathbb{T}_1^4 = 0, \\ \left(\frac{\partial p}{\partial t} + \rho c \frac{\partial u_1}{\partial t}\right) + \mathcal{L}_5 - \mathbb{T}_1^5 = 0, \\ \frac{\partial Z}{\partial t} + \mathcal{L}_6 - \mathbb{T}_1^6 = 0, \end{cases} \tag{15}$$

where $\mathbb{T}_k^m$ indicates a characteristic transverse term in the plane perpendicular to x_k relevant to the mth characteristic variable

$$\begin{cases} \mathbb{T}_1^1 = \mathcal{T}_5 - \rho c \mathcal{T}_2, \\ \mathbb{T}_1^2 = c^2 \mathcal{T}_1 - \mathcal{T}_5, \\ \mathbb{T}_1^3 = \mathcal{T}_3, \\ \mathbb{T}_1^4 = \mathcal{T}_4, \\ \mathbb{T}_1^5 = \mathcal{T}_5 + \rho c \mathcal{T}_2, \\ \mathbb{T}_1^6 = \mathcal{T}_6. \end{cases} \tag{16}$$

3.1.1. Subsonic non-reflecting outflow

The physical boundary condition, which links primitive variables to wave amplitudes, is obtained from the pressure relaxation condition proposed by Rudy and Strikwerda [15] with an additional transverse relaxation term as discussed by Yoo et al. [24]. The waves velocities are given by Eqs. (A.8)–(A.10) and depending on their sign, $\mathcal{L}_i$ are entering (unknown and needing an equation to be determined) or leaving the domain

(known). For boundaries orthogonal to x_1, depending on their location, the unknown incoming wave is either $\mathcal{L}_1$ (at $x_1 = L_x$) or $\mathcal{L}_5$ (at $x_1 = 0$). The relevant boundary condition can be conveniently expressed as follows:

$$\left(\frac{\partial p}{\partial t} + \varsigma\rho c\frac{\partial u_1}{\partial t}\right) + \sigma\frac{c(1-\mathscr{M}^2)}{L_x}(p - p_\infty) - \beta(\mathbb{T}_1^\phi - \mathbb{T}_{1,\mathrm{ex}}^\phi) = 0, \tag{17}$$

where σ is the pressure relaxation coefficient, $\mathscr{M}$ is the maximum Mach number, L_x is the characteristic size of the computational domain along x_1 and $\beta \in [0:1]$ is a transverse damping parameter. ς is a function which sets the correct sign for the velocity term depending on the value of the wave index ϕ:

$$\varsigma(\phi) = \frac{\phi - 1}{2} - 1 = \begin{cases} -1 & \text{if } \phi = 1, \\ +1 & \text{if } \phi = 5. \end{cases} \tag{18}$$

For most free shear flows, the boundary condition is expected to well behave with $\mathbb{T}_{1,\mathrm{ex}}^\phi = 0$, as shown in the next section. However, when an analytical steady solution of the flow is known at the boundary, the target value of the transverse term $\mathbb{T}_{1,\mathrm{ex}}^\phi$ is obtained applying equations (14) and (16):

$$\Rightarrow \mathbb{T}_{1,\mathrm{ex}}^\phi = -\hat{u}_t\frac{\partial \hat{p}}{\partial x_t} - \gamma\hat{p}\frac{\partial \hat{u}_t}{\partial x_t} - \varsigma\hat{\rho}\hat{c}\hat{u}_t\frac{\partial \hat{u}_1}{\partial x_t} \quad (t = 2, 3), \tag{19}$$

where the $\hat{(\cdot)}$ accent indicates the known analytical solution for the target flow.

Combining Eq. (17) with the corresponding characteristic equation from system (15), the unknown incoming wave becomes

$$\mathcal{L}_\phi = \sigma\frac{c(1-\mathscr{M}^2)}{L_x}(p - p_\infty) + (1-\beta)\mathbb{T}_1^\phi + \beta\mathbb{T}_{1,\mathrm{ex}}^\phi \tag{20}$$

with

$$\mathbb{T}_1^\phi = \mathcal{T}_5 + \varsigma\rho c\mathcal{T}_2. \tag{21}$$

Navier–Stokes boundary conditions are obtained by complementing the above inviscid condition with the following viscous conditions:

$$\frac{\partial \tau_{12}}{\partial x_1} = \frac{\partial \tau_{13}}{\partial x_1} = \frac{\partial q_1}{\partial x_1} = \frac{\partial}{\partial x_1}\left(\rho D\frac{\partial Z}{\partial x_1}\right) = 0. \tag{22}$$

3.1.2. Subsonic non-reflecting inflow

The procedure of Yoo et al. [24] is followed for inflow, away from edges and corner. The inlet is composed of five entering waves, leading to five closures for boundary conditions. Here it is chosen to impose temperature and velocity and passive scalar; other choices are possible like density or mass flow rate that will not be discussed here. The closed system reads

$$\left(\frac{\partial p}{\partial t} + \varsigma\rho c\frac{\partial u_1}{\partial t}\right) + \eta_\phi\frac{\rho c^2(1-\mathscr{M}^2)}{L_x}(u_1 - u_{1_0}) = 0, \tag{23}$$

$$\left(c^2\frac{\partial \rho}{\partial t} - \frac{\partial p}{\partial t}\right) + \eta_2\frac{\rho c\mathcal{R}}{L_x}(T - T_0) = 0, \tag{24}$$

$$\frac{\partial u_2}{\partial t} + \eta_3\frac{c}{L_x}(u_2 - u_{2_0}) = 0, \tag{25}$$

$$\frac{\partial u_3}{\partial t} + \eta_4\frac{c}{L_x}(u_3 - u_{3_0}) = 0, \tag{26}$$

$$\frac{\partial Z}{\partial t} + \eta_6\frac{c}{L_x}(Z - Z_0) = 0 \tag{27}$$

with $\eta_1, \ldots, \eta_6$ relaxation parameters (η_1 and η_2 negative) and the subscript 0 denoting target values for the relevant quantities. In Eq. (23) the index ϕ is equal to 1 or 5 depending whether the inlet is located at $x_1 = L_x$ or $x_1 = 0$, respectively; ς sets the sign accordingly (Eq. (18)).

The equations for the unknown entering wave amplitudes are obtained from system (15) closed with Eqs. (23)–(27):

$$\mathcal{L}_\phi = \eta_\phi \frac{\rho c^2 (1-\mathscr{M}^2)}{L_x}(u_1 - u_{1_0}) + (\mathcal{T}_5 + \varsigma \rho c \mathcal{T}_2), \tag{28}$$

$$\mathcal{L}_2 = \eta_2 \frac{\rho c \mathcal{R}}{L_x}(T - T_0) + (c^2 \mathcal{T}_1 - \mathcal{T}_5), \tag{29}$$

$$\mathcal{L}_3 = \eta_3 \frac{c}{L_x}(u_2 - u_{2_0}) + \mathcal{T}_3, \tag{30}$$

$$\mathcal{L}_4 = \eta_4 \frac{c}{L_x}(u_3 - u_{3_0}) + \mathcal{T}_4, \tag{31}$$

$$\mathcal{L}_6 = \eta_6 \frac{c}{L_x}(Z - Z_0) + \mathcal{T}_6. \tag{32}$$

It should be noted that this particular inflow condition does not require any additional viscous condition as the density ρ—the only remaining unknown—is obtained from the continuity equation, which does not involve any viscous term [12].

3.2. Edge boundaries

Supposing that the edge is aligned along x_3 (face boundaries composing the edge are normal to x_1 and x_2), the system linking primitive variables with amplitude of the waves $\mathcal{L}_i$ and $\mathcal{M}_i$, traveling in both directions x_1 and x_2 is obtained from a two-dimensional characteristic analysis (Eq. (A.27)) by neglecting the $\boldsymbol{D}$ term only:

$$\begin{cases} \frac{\partial \rho}{\partial t} + \frac{1}{c^2}\left[\mathcal{L}_2 + \frac{1}{2}(\mathcal{L}_5 + \mathcal{L}_1)\right] + \frac{1}{c^2}\left[\mathcal{M}_3 + \frac{1}{2}(\mathcal{M}_5 + \mathcal{M}_1)\right] - \mathcal{T}_1 = 0, \\ \frac{\partial u_1}{\partial t} + \frac{1}{2\rho c}(\mathcal{L}_5 - \mathcal{L}_1) + \mathcal{M}_2 - \mathcal{T}_2 = 0, \\ \frac{\partial u_2}{\partial t} + \mathcal{L}_3 + \frac{1}{2\rho c}(\mathcal{M}_5 - \mathcal{M}_1) - \mathcal{T}_3 = 0, \\ \frac{\partial u_3}{\partial t} + \mathcal{L}_4 + \mathcal{M}_4 - \mathcal{T}_4 = 0, \\ \frac{\partial p}{\partial t} + \frac{1}{2}(\mathcal{L}_5 + \mathcal{L}_1) + \frac{1}{2}(\mathcal{M}_5 + \mathcal{M}_1) - \mathcal{T}_5 = 0, \\ \frac{\partial Z}{\partial t} + \mathcal{L}_6 + \mathcal{M}_6 - \mathcal{T}_6 = 0 \end{cases} \tag{33}$$

with

$$\boldsymbol{\mathcal{T}} = \begin{pmatrix} -\frac{\partial m_3}{\partial x_3} \\ -u_3 \frac{\partial u_1}{\partial x_3} \\ -u_3 \frac{\partial u_2}{\partial x_3} \\ -u_3 \frac{\partial u_3}{\partial x_3} - \frac{1}{\rho}\frac{\partial p}{\partial x_3} \\ -u_3 \frac{\partial p}{\partial x_3} - \gamma p \frac{\partial u_3}{\partial x_3} \\ -u_3 \frac{\partial Z}{\partial x_3} \end{pmatrix}. \tag{34}$$

A procedure similar to the one discussed for face boundaries may be used. System (33) is combined with physical boundary conditions to compute the unknown incoming wave amplitude variations of both boundaries. These wave amplitude variations are now coupled, therefore, in general, a linear system in the unknown waves has to be solved. An additional problem arises when the boundaries sharing the edge are of different kind; in this case, not only different characteristic directions have to be considered simultaneously but, depending on the boundary types, additional compatibility conditions must be introduced to ensure numerical stability.

Note that the wall boundary condition presented in what follows is always considered as adiabatic no-slip, therefore, the relevant inviscid conditions are augmented by the addition of the following viscous conditions:

$$q_n = 0, \quad \rho D \frac{\partial Z}{\partial x_n} = 0, \tag{35}$$

subscript n indicating the direction normal to the wall. Viscous conditions for inflow and outflow boundaries are enforced as for face boundaries (see Sections 3.1.1 and 3.1.2).

3.2.1. Outflow/outflow edge

Two characteristic-type relations may be written combining the second, the third and the fifth equations in system (33):

$$\left(\frac{\partial p}{\partial t}+\varsigma(\phi)\rho c\frac{\partial u_1}{\partial t}\right)+\mathcal{L}_\phi+\underbrace{\frac{\mathcal{M}_5+\mathcal{M}_1}{2}-\mathcal{T}_5+\varsigma(\phi)\rho c(\mathcal{M}_2-\mathcal{T}_2)}_{-\mathbb{T}_1^\phi}=0, \tag{36}$$

$$\left(\frac{\partial p}{\partial t}+\varsigma(\psi)\rho c\frac{\partial u_2}{\partial t}\right)+\mathcal{M}_\psi+\underbrace{\frac{\mathcal{L}_5+\mathcal{L}_1}{2}-\mathcal{T}_5+\varsigma(\psi)\rho c(\mathcal{L}_3-\mathcal{T}_3)}_{-\mathbb{T}_2^\psi}=0, \tag{37}$$

where ϕ and ψ are indices taking either the values 1 or 5 depending on the location of the edge as summarized in Table 1; ς is the switch defined in Eq. (18).

The boundary conditions are obtained from Eq. (17) written for u_1 and u_2:

$$\left(\frac{\partial p}{\partial t}+\varsigma(\phi)\rho c\frac{\partial u_1}{\partial t}\right)+\sigma\frac{c(1-\mathscr{M}^2)}{L_x}(p-p_\infty)-\beta(\mathbb{T}_1^\phi-\mathbb{T}_{1,\mathrm{ex}}^\phi)=0, \tag{38}$$

$$\left(\frac{\partial p}{\partial t}+\varsigma(\psi)\rho c\frac{\partial u_2}{\partial t}\right)+\sigma\frac{c(1-\mathscr{M}^2)}{L_y}(p-p_\infty)-\beta(\mathbb{T}_2^\psi-\mathbb{T}_{2,\mathrm{ex}}^\psi)=0, \tag{39}$$

where $\mathbb{T}_{1,\mathrm{ex}}^\phi$ and $\mathbb{T}_{2,\mathrm{ex}}^\psi$ may be computed from a reference steady flow by applying definition (14) written for boundaries orthogonal to x_1 and x_2, respectively:

$$\mathbb{T}_{1,\mathrm{ex}}^\phi=-\hat{u}_t\frac{\partial\hat{p}}{\partial x_t}-\gamma\hat{p}\frac{\partial\hat{u}_t}{\partial x_t}-\varsigma(\phi)\hat{\rho}\hat{c}\hat{u}_t\frac{\partial\hat{u}_1}{\partial x_t}\quad(t=2,3), \tag{40}$$

$$\mathbb{T}_{2,\mathrm{ex}}^\psi=-\hat{u}_t\frac{\partial\hat{p}}{\partial x_t}-\gamma\hat{p}\frac{\partial\hat{u}_t}{\partial x_t}-\varsigma(\psi)\hat{\rho}\hat{c}\hat{u}_t\frac{\partial\hat{u}_2}{\partial x_t}\quad(t=1,3). \tag{41}$$

From Eqs. (36)–(39), the unknown waves are then solution of the system:

$$\begin{cases}\mathcal{L}_\phi+\frac{1-\beta}{2}\mathcal{M}_\psi=\sigma\dfrac{c(1-\mathscr{M}^2)}{L_x}(p-p_\infty)+(1-\beta)\widetilde{\mathbb{T}}_1^\phi+\beta\mathbb{T}_{1,\mathrm{ex}}^\phi,\\ \frac{1-\beta}{2}\mathcal{L}_\phi+\mathcal{M}_\psi=\sigma\dfrac{c(1-\mathscr{M}^2)}{L_y}(p-p_\infty)+(1-\beta)\widetilde{\mathbb{T}}_2^\psi+\beta\mathbb{T}_{2,\mathrm{ex}}^\psi\end{cases} \tag{42}$$

with the known terms

$$\widetilde{\mathbb{T}}_1^\phi=\mathcal{T}_5-\frac{\mathcal{M}_{\psi^*}}{2}-\varsigma(\phi)\rho c(\mathcal{M}_2-\mathcal{T}_2), \tag{43}$$

$$\widetilde{\mathbb{T}}_2^\psi=\mathcal{T}_5-\frac{\mathcal{L}_{\phi^*}}{2}-\varsigma(\psi)\rho c(\mathcal{L}_3-\mathcal{T}_3), \tag{44}$$

Table 1
Values of the indices ϕ and ψ depending on edge location

x_2 \ x_1	ϕ	ψ	ϕ	ψ
	0		L_x	
0	5	5	1	5
L_y	5	1	1	1

where $\phi^* = 6 - \phi$ and $\psi^* = 6 - \psi$. It should be noted that, since $0 \leqslant \beta \leqslant 1$, system (42) always admits solution, the determinant of the relevant matrix of coefficient being zero for $\beta = -1$ and $\beta = 3$; nonetheless, some care has to be taken in general as, depending on the particular boundaries considered, a check on this regard is recommended.

3.2.2. Inflow/outflow edge

An analogous procedure as the one used for the outflow/outflow boundary edge could be followed in this case. On the inflow/outflow edge, in fact, there are five incoming waves on the inflow side and one incoming wave on the outflow side for a total number of six physical boundary conditions. Therefore, inlet and outlet boundary conditions could be, in principle, simultaneously imposed. Nonetheless, even allowing smooth transients for pressure, the two boundary conditions have shown problems of stability when simultaneously imposed. A simple remedy, which has proven effective for the configurations studied in this work, is to set to zero the incoming wave amplitude relevant to the outflow boundary ("perfectly non-reflecting" outflow). In this way, the pressure is left free to adapt to the local flow field and tends anyway to the expected value due to the effect of the neighboring regions. Furthermore, as the only unknown wave amplitude on the outflow side is directly imposed, the edge become uncoupled on the two characteristic directions and the remaining incoming waves can be computed directly from system (33) and Eqs. (23)–(27).

Supposing for instance the inlet normal to x_1 and the outflow normal to x_2, the expression for the unknown wave amplitude variations are

$$\mathcal{M}_\psi = 0 \quad \text{(compatibility condition)}, \tag{45}$$

$$\mathcal{L}_\phi = \eta_\phi \frac{\rho c^2 (1 - \mathscr{M}^2)}{L_x}(u_1 - u_{1_0}) - \frac{\mathcal{M}_{\psi^*}}{2} + \mathcal{T}_5 + \varsigma(\phi)\rho c(\mathcal{T}_2 - \mathcal{M}_2), \tag{46}$$

$$\mathcal{L}_2 = \eta_2 \frac{\rho c \mathcal{R}}{L_x}(T - T_0) - \mathcal{M}_3 + (c^2 \mathcal{T}_1 - \mathcal{T}_5), \tag{47}$$

$$\mathcal{L}_3 = \eta_3 \frac{c}{L_x}(u_2 - u_{2_0}) + \frac{\varsigma(\psi)}{2\rho c}\mathcal{M}_{\psi^*} + \mathcal{T}_3, \tag{48}$$

$$\mathcal{L}_4 = \eta_4 \frac{c}{L_x}(u_3 - u_{3_0}) - \mathcal{M}_4 + \mathcal{T}_4, \tag{49}$$

$$\mathcal{L}_6 = \eta_6 \frac{c}{L_x}(Z - Z_0) - \mathcal{M}_6 + \mathcal{T}_6, \tag{50}$$

where the indices ϕ and ψ and the value of ς can be obtained from Table 1 and Eq. (18) and $\psi^* = 6 - \psi$. The equation for $\mathcal{L}_3$ has been obtained using the following identity:

$$\frac{1}{2\rho c}(\mathcal{M}_5 - \mathcal{M}_1) = \frac{\varsigma(\psi)}{2\rho c}(\mathcal{M}_\psi - \mathcal{M}_{\psi^*}). \tag{51}$$

3.2.3. Wall/outflow edge

On this kind of edge, in principle, one should impose the pressure for what concerns the outlet condition, and velocity for what concerns the wall condition (the time derivative of the velocity component normal to the wall is set to zero). As suggested by Poinsot and Lele [12], just imposing all these quantities at the same time is not effective, but allowing smooth transient for the pressure, namely relaxing outlet pressure, improves the stability of the boundary condition.

Let the wall be normal to x_1 and the outflow be normal to x_2. Since the velocity at the wall is zero, the only non-zero wave amplitude variations are $\mathcal{L}_{1,5}$ and $\mathcal{M}_{1,5}$ (those characterized by characteristic speeds $u_1 \mp c$ and $u_2 \mp c$, respectively). $\mathcal{T}_1$, $\mathcal{T}_2$, $\mathcal{T}_3$ and $\mathcal{T}_5$ are zero as well. The physical boundary conditions are expressed by

$$\frac{\partial u_1}{\partial t} = 0 \tag{52}$$

and Eq. (17) (written for u_2). From system (33) the relevant equations are

$$\frac{\partial u_1}{\partial t}+\frac{1}{2\rho c}(\mathcal{L}_5-\mathcal{L}_1)=0, \tag{53}$$

$$\left(\frac{\partial p}{\partial t}+\varsigma(\psi)\rho c\frac{\partial u_2}{\partial t}\right)+\mathcal{M}_\psi+\underbrace{\frac{1}{2}(\mathcal{L}_5+\mathcal{L}_1)}_{-\mathbb{T}_2^\psi}=0 \tag{54}$$

and the solving system for the unknown $\mathcal{L}_\phi$ and $\mathcal{M}_\psi$ reads

$$\begin{cases}\mathcal{L}_\phi=\mathcal{L}_{\phi^*},\\ \mathcal{M}_\psi=\sigma\frac{c(1-\mathscr{M}^2)}{L_y}(p-p_\infty)-(1-\beta)\mathcal{L}_{\phi^*}+\beta\mathbb{T}_{2,\mathrm{ex}}^\psi\end{cases} \tag{55}$$

with $\phi^*=6-\phi$. Velocity components u_2 and u_3 are simply forced to zero and $\mathbb{T}_{2,\mathrm{ex}}^\psi$ is expressed by Eq. (41).

3.3. Corner boundaries

The system relating primitive variables with the characteristic waves is obtained from Eq. (A.38) by neglecting the $\boldsymbol{D}$ term as before

$$\begin{cases}\frac{\partial\rho}{\partial t}+\frac{1}{c^2}\left[\mathcal{L}_2+\frac{1}{2}(\mathcal{L}_5+\mathcal{L}_1)\right]+\frac{1}{c^2}\left[\mathcal{M}_3+\frac{1}{2}(\mathcal{M}_5+\mathcal{M}_1)\right]+\frac{1}{c^2}\left[\mathcal{N}_4+\frac{1}{2}(\mathcal{N}_5+\mathcal{N}_1)\right]=0,\\ \frac{\partial u_1}{\partial t}+\frac{1}{2\rho c}(\mathcal{L}_5-\mathcal{L}_1)+\mathcal{M}_2+\mathcal{N}_2=0,\\ \frac{\partial u_2}{\partial t}+\mathcal{L}_3+\frac{1}{2\rho c}(\mathcal{M}_5-\mathcal{M}_1)+\mathcal{N}_3=0,\\ \frac{\partial u_3}{\partial t}+\mathcal{L}_4+\mathcal{M}_4+\frac{1}{2\rho c}(\mathcal{N}_5-\mathcal{N}_1)=0,\\ \frac{\partial p}{\partial t}+\frac{1}{2}(\mathcal{L}_5+\mathcal{L}_1)+\frac{1}{2}(\mathcal{M}_5+\mathcal{M}_1)+\frac{1}{2}(\mathcal{N}_5+\mathcal{N}_1)=0,\\ \frac{\partial Z}{\partial t}+\mathcal{L}_6+\mathcal{M}_6+\mathcal{N}_6=0.\end{cases} \tag{56}$$

The procedure is similar to the one used for face and edge boundaries, except that in this case all the transverse terms are expressed by wave amplitude variations. Once the incoming waves are solved using physical boundary conditions, viscous conditions are enforced and the boundary nodes are advanced in time.

As in Section 3.2, we will only consider adiabatic no-slip wall boundary conditions and the relevant additional viscous conditions are obtained from Eq. (35). Viscous conditions for inflow and outflow boundaries are enforced as for face boundaries (see Sections 3.1.1 and 3.1.2).

3.3.1. Wall/outflow/outflow corner

Let the wall be normal to x_1 and the outflows be normal to x_2 and x_3. Since the velocity at the wall is zero, the only non-zero wave amplitude variations are $\mathcal{L}_{1,5}$, $\mathcal{M}_{1,5}$ and $\mathcal{N}_{1,5}$ (those characterized by characteristic speeds $u_1\mp c$, $u_2\mp c$ and $u_3\mp c$, respectively). The boundary conditions are expressed by Eq. (17) (written for u_2 and u_3) and Eq. (52). From system (56) the equations to be considered are

$$\frac{\partial u_1}{\partial t}+\frac{1}{2\rho c}(\mathcal{L}_5-\mathcal{L}_1)=0, \tag{57}$$

$$\left(\frac{\partial p}{\partial t}+\varsigma(\psi)\rho c\frac{\partial u_2}{\partial t}\right)+\mathcal{M}_\psi+\underbrace{\frac{\mathcal{L}_5+\mathcal{L}_1+\mathcal{N}_5+\mathcal{N}_1}{2}}_{-\mathbb{T}_2^\psi}=0, \tag{58}$$

$$\left(\frac{\partial p}{\partial t}+\varsigma(\chi)\rho c\frac{\partial u_3}{\partial t}\right)+\mathcal{N}_\chi+\underbrace{\frac{\mathcal{L}_5+\mathcal{L}_1+\mathcal{M}_5+\mathcal{M}_1}{2}}_{-\mathbb{T}_3^\chi}=0, \tag{59}$$

where ψ and χ are indices taking either the values 1 or 5 depending on the location of the corner and ς is the switch defined by Eq. (18). In particular, ψ is obtained from Table 1 and χ, by analogy, is equal to 1 for $x_3=L_z$ and 5 for $x_3=0$. The incoming wave relevant to the wall condition is readily solved by setting $\mathcal{L}_1=\mathcal{L}_5$; there-

fore, the remaining unknown waves can be solved by applying a procedure similar to the one described for outflow/outflow edges. The solving system then reads

$$\begin{cases} \mathcal{L}_\phi = \mathcal{L}_{\phi^*}, \\ \mathcal{M}_\psi + \frac{1-\beta}{2}\mathcal{N}_\chi = \sigma\frac{c(1-\mathscr{M}^2)}{L_y}(p-p_\infty) + (1-\beta)\widetilde{\mathbb{T}}_2^\psi + \beta\mathbb{T}_{2,\mathrm{ex}}^\psi, \\ \frac{1-\beta}{2}\mathcal{M}_\psi + \mathcal{N}_\chi = \sigma\frac{c(1-\mathscr{M}^2)}{L_z}(p-p_\infty) + (1-\beta)\widetilde{\mathbb{T}}_3^\chi + \beta\mathbb{T}_{3,\mathrm{ex}}^\chi \end{cases} \tag{60}$$

with $\mathbb{T}_{2,\mathrm{ex}}^\psi$ computed from Eq. (41) and

$$\widetilde{\mathbb{T}}_2^\psi = -\mathcal{L}_{\phi^*} - \frac{1}{2}\mathcal{N}_{\chi^*}, \tag{61}$$

$$\widetilde{\mathbb{T}}_3^\chi = -\mathcal{L}_{\phi^*} - \frac{1}{2}\mathcal{M}_{\psi^*}, \tag{62}$$

$$\mathbb{T}_{3,\mathrm{ex}}^\chi = -\hat{u}_t\frac{\partial\hat{p}}{\partial x_t} - \gamma\hat{p}\frac{\partial\hat{u}_t}{\partial x_t} - \varsigma(\chi)\hat{\rho}\hat{c}\hat{u}_t\frac{\partial\hat{u}_3}{\partial x_t} \quad (t=1,2), \tag{63}$$

where $\phi^* = 6-\phi$, $\psi^* = 6-\psi$ and $\chi^* = 6-\chi$.

3.3.2. Inflow/outflow/outflow corner

The presence of the inlet condition makes it necessary to impose compatibility conditions. In analogy to what is done on inflow/outflow boundaries, the "perfectly non-reflecting" condition is imposed on the outflows, thus decoupling the inlet from the outlets.

Let the inflow be normal to x_1 and the outflows be normal to x_2 and x_3, respectively. Then, the compatibility conditions are

$$\mathcal{M}_\psi = 0, \tag{64}$$

$$\mathcal{N}_\chi = 0 \tag{65}$$

and the unknown wave amplitude variations on the inflow side are directly solved from the system (56) and the boundary conditions (23)–(27):

$$\mathcal{L}_\phi = \eta_\phi\frac{\rho c^2(1-\mathscr{M}^2)}{L_x}(u_1-u_{1_0}) - \frac{\mathcal{M}_{\psi^*}+\mathcal{N}_{\chi^*}}{2} - \varsigma(\phi)\rho c(\mathcal{M}_2+\mathcal{N}_2), \tag{66}$$

$$\mathcal{L}_2 = \eta_2\frac{\rho c\mathcal{R}}{L_x}(T-T_0) - \mathcal{M}_3 - \mathcal{N}_4, \tag{67}$$

$$\mathcal{L}_3 = \eta_3\frac{c}{L_x}(u_2-u_{2_0}) + \frac{\varsigma(\psi)}{2\rho c}\mathcal{M}_{\psi^*} - \mathcal{N}_3, \tag{68}$$

$$\mathcal{L}_4 = \eta_4\frac{c}{L_x}(u_3-u_{3_0}) + \frac{\varsigma(\chi)}{2\rho c}\mathcal{N}_{\chi^*} - \mathcal{M}_4, \tag{69}$$

$$\mathcal{L}_6 = \eta_6\frac{c}{L_x}(Z-Z_0) - \mathcal{M}_6 - \mathcal{N}_6 \tag{70}$$

with $\psi^* = 6-\psi$ and $\chi^* = 6-\chi$. An analogous identity as in Eq. (51) has been used to derive the equation for $\mathcal{L}_4$.

3.3.3. Outflow/outflow/outflow corner

The three characteristic equations relevant to the unknown wave amplitude variations are obtained from system (56):

$$\left(\frac{\partial p}{\partial t} + \varsigma(\phi)\rho c\frac{\partial u_1}{\partial t}\right) + \mathcal{L}_\phi + \underbrace{\frac{\mathcal{M}_5+\mathcal{M}_1+\mathcal{N}_5+\mathcal{N}_1}{2} + \varsigma(\phi)\rho c(\mathcal{M}_2+\mathcal{N}_2)}_{-\mathbb{T}_1^\phi} = 0, \tag{71}$$

$$\left(\frac{\partial p}{\partial t}+\varsigma(\psi)\rho c\frac{\partial u_2}{\partial t}\right)+\mathcal{M}_\psi+\underbrace{\frac{\mathcal{L}_5+\mathcal{L}_1+\mathcal{N}_5+\mathcal{N}_1}{2}+\varsigma(\psi)\rho c(\mathcal{L}_3+\mathcal{N}_3)}_{-\mathbb{T}_2^\psi}=0, \tag{72}$$

$$\left(\frac{\partial p}{\partial t}+\varsigma(\chi)\rho c\frac{\partial u_3}{\partial t}\right)+\mathcal{N}_\chi+\underbrace{\frac{\mathcal{L}_5+\mathcal{L}_1+\mathcal{M}_5+\mathcal{M}_1}{2}+\varsigma(\chi)\rho c(\mathcal{L}_4+\mathcal{M}_4)}_{-\mathbb{T}_3^\chi}=0. \tag{73}$$

The three necessary boundary conditions are obtained from Eq. (17) plus analogous relations for u_2 and u_3. The unknown waves are then computed by solving the following system:

$$\begin{cases}\mathcal{L}_\phi+\frac{1-\beta}{2}\mathcal{M}_\psi+\frac{1-\beta}{2}\mathcal{N}_\chi=\sigma\frac{c\left(1-\mathscr{M}^2\right)}{L_x}(p-p_\infty)+(1-\beta)\widetilde{\mathbb{T}}_1^\phi+\beta\mathbb{T}_{1,\mathrm{ex}}^\phi,\\ \frac{1-\beta}{2}\mathcal{L}_\phi+\mathcal{M}_\psi+\frac{1-\beta}{2}\mathcal{N}_\chi=\sigma\frac{c\left(1-\mathscr{M}^2\right)}{L_y}(p-p_\infty)+(1-\beta)\widetilde{\mathbb{T}}_2^\psi+\beta\mathbb{T}_{2,\mathrm{ex}}^\psi,\\ \frac{1-\beta}{2}\mathcal{L}_\phi+\frac{1-\beta}{2}\mathcal{M}_\psi+\mathcal{N}_\chi=\sigma\frac{c\left(1-\mathscr{M}^2\right)}{L_z}(p-p_\infty)+(1-\beta)\widetilde{\mathbb{T}}_3^\chi+\beta\mathbb{T}_{3,\mathrm{ex}}^\chi\end{cases} \tag{74}$$

with $\mathbb{T}_{1,\mathrm{ex}}^\phi$, $\mathbb{T}_{2,\mathrm{ex}}^\psi$ and $\mathbb{T}_{3,\mathrm{ex}}^\chi$ obtained from Eqs. (40), (41) and (63), respectively and

$$\widetilde{\mathbb{T}}_1^\phi=-\frac{\mathcal{M}_{\psi^*}+\mathcal{N}_{\chi^*}}{2}-\varsigma(\phi)\rho c(\mathcal{M}_2+\mathcal{N}_2), \tag{75}$$

$$\widetilde{\mathbb{T}}_2^\psi=-\frac{\mathcal{L}_{\phi^*}+\mathcal{N}_{\chi^*}}{2}-\varsigma(\psi)\rho c(\mathcal{L}_3+\mathcal{N}_3), \tag{76}$$

$$\widetilde{\mathbb{T}}_3^\chi=-\frac{\mathcal{L}_{\phi^*}+\mathcal{M}_{\psi^*}}{2}-\varsigma(\chi)\rho c(\mathcal{L}_4+\mathcal{M}_4), \tag{77}$$

where $\phi^*=6-\phi$, $\psi^*=6-\psi$ and $\chi^*=6-\chi$. Observe that the determinant of the relevant coefficients matrix is $-\frac{1}{4}\beta^3+\frac{3}{4}\beta+\frac{1}{2}$ and is zero for $\beta=-1$ (two coincident roots) and $\beta=2$, therefore, system (74) always admits solution for $\beta\in[0:1]$.

4. Results

Tests of 3D-NSCBC have been performed by means of a parallel solver based on the explicit finite volumes (FV) scheme for cartesian grids. The convective terms are computed resorting to the fourth-order centered skew-symmetric-like scheme proposed by Ducros et al. [4], while the diffusive terms are computed using a fourth-order centered scheme. In LES tests, a blend of second- and fourth-order artificial dissipation terms [20,18] is added in order to suppress spurious oscillations and damp high-frequency modes. Time integration is performed using a third-order Runge–Kutta scheme [7]. Within the framework of the FV scheme, the boundary problem reduces to the computation of boundary fluxes. On the other hand, the NSCBC approach is generally well suited for finite differences (FD) schemes, therefore its implementation, in the present case, requires the use of a hybrid FV–FD scheme at the boundary. We compute, then, boundary fluxes using values of the flow variables computed on an extra grid point located at the center of each computational cell's boundary face, the extra nodes being computed using the FD approach in order to integrate the relevant equation in conservative form (see Eqs. (A.18), (A.28) and (A.39)).

All the tests presented in the following sections have been performed using air and the relevant properties are summarized in Table 2.

4.1. Single vortex test-case

The first test is the two-dimensional compressible vortex convected through a non-reflecting boundary. This is a typical test used to evaluate boundary conditions and it is particularly suited to assess non-reflecting outflows for turbulent flow simulations. The configuration corresponds to a single vortex superimposed on a uniform flow field aligned along the x_1-direction. The initial flow field is defined in terms of the stream function as

Table 2
Air properties

	Value	Ref.
M_w	28.9×10^{-3} kg/mol	Eq. (5)
γ	1.4	Eq. (9)
Pr	0.72	Eq. (12)
Sc	0.72	Eq. (12)
Pr_T	0.90	
Sc_T	0.90	
μ_{ref}	1.827×10^{-5} kg/(m s)	Eq. (11)
T_{ref}	291.15 K	Eq. (11)
S	120.0 K	Eq. (11)

Pr_T and Sc_T are the turbulent Prandtl and Schmidt numbers, respectively, which have been used in LES computations.

$$\Psi = C_v \exp\left(-\frac{r^2}{2R_v^2}\right) + U_0 x_2, \tag{78}$$

$$u_1 = \frac{\partial \Psi}{\partial x_2}, \tag{79}$$

$$u_2 = -\frac{\partial \Psi}{\partial x_1}, \tag{80}$$

where C_v is the vortex strength, $r = \sqrt{x_1^2 + x_2^2}$ is the radial distance from the reference frame's x_3 axis and R_v is the vortex radius. U_0 is the speed of the uniform flow field along x_1. The pressure, density and temperature can be obtained from an analytical solution. In fact, it can be shown [3] that the pressure distribution is solution of

$$\frac{\partial p}{\partial r} = \frac{\rho u_\theta^2}{r}, \tag{81}$$

where u_θ is the tangential velocity field in a reference frame attached to the vortex center:

$$u_\theta = \frac{C_v r}{R_v^2} \exp\left(-\frac{r^2}{2R_v^2}\right). \tag{82}$$

Assuming that the temperature is constant and equal to T_0, the initial pressure and density distributions can be computed as

$$p(r) = p_\infty \exp\left[-\frac{\gamma}{2}\left(\frac{C_v}{cR_v}\right)^2 \exp\left(-\frac{r^2}{R_v^2}\right)\right], \tag{83}$$

$$\rho(r) = \frac{p(r)}{\mathcal{R}T_0} \tag{84}$$

with $c = \sqrt{\gamma \mathcal{R} T_0}$ the sound speed.

For the present tests, C_v was set at 5×10^{-3} m^2/s, R_v was set at 10% of the domain size L; p_∞ and T_0 were 1 atm, and 300 K, respectively.

Three test-cases are presented with U_0 equal to 2 m/s, 200 m/s and 300 m/s, respectively, in order to assess 3D-NSCBC at different Mach numbers ($Ma = 0.00575$, 0.575 and 0.863, respectively, based on the velocity U_0). The Reynolds number (computed from the velocity U_0 and the vortex radius R_v) for the three tests is about 166, 16,600 and 24,900, respectively.

The computational domain is a square of dimension $L = 0.013$ m with uniform U_0 inlet velocity at the left ($x_1 = -0.0065$ m) boundary, and non-reflecting outflow at the right boundary; the relaxation parameter for pressure σ was equal to 0.28 for all the tests, which corresponds to the optimal value proposed by Rudy and Strikwerda [15]. Increasing this value leads to a more reflective boundary condition. All the other boundaries were periodic.

Figs. 1–3 show a comparison of results obtained using the standard NSCBC non-reflecting outflow and the 3D-NSCBC. The represented quantities are the pressure field, the vorticity contours, the longitudinal velocity contours and the contours of the velocity gradient tensor invariant Q defined as

$$Q = -\frac{1}{2}\frac{\partial u_i}{\partial x_j}\frac{\partial u_j}{\partial x_i} = -\frac{1}{2}\left(S_{ij}S_{ij} - \frac{1}{2}\boldsymbol{\omega}^2\right), \tag{85}$$

where S_{ij} is the strain tensor and $\boldsymbol{\omega}$ is the vorticity vector (ϵ_{kij} is the Levi–Civita symbol):

$$S_{ij} = \frac{1}{2}\left(\frac{\partial u_i}{\partial x_j} + \frac{\partial u_j}{\partial x_i}\right), \tag{86}$$

$$\omega_i = \epsilon_{ijk}\frac{\partial u_k}{\partial x_j}. \tag{87}$$

The frames have been taken at three different times and each figure refers to a different Mach number test. The pressure, in particular, is expressed in terms of its relative value, with respect to the far field pressure p_∞, normalized by the initial maximum pressure drop at the center of the vortex:

$$p^*(\boldsymbol{x}, t) = \frac{p(\boldsymbol{x}, t) - p_\infty}{p(\mathbf{0}, 0) - p_\infty}. \tag{88}$$

The initial map of p^* is then expected to be equal to 1 in the vortex center and 0 in the far field; once the vortex has left the domain, p^* is expected to be identically 0 all over the domain.

All the computations have been done setting $\mathbb{T}^1_{1,\mathrm{ex}} = 0$ (see Eq. (20)); it is interesting to note that, under this particular assumption—motivated by the fact that no transverse terms are expected for such a flow after the vortex has left the domain—the standard LODI assumption is retrieved in the limit of the transverse damping parameter β equal to 1. On the other hand, from numerical tests performed, it appears that in general the optimal value for β is related to the typical Mach number for the specific flow. For the vortex problem, indeed, the best choice for the transverse relaxation coefficient is

$$\beta \simeq Ma = \frac{U_0}{\sqrt{\gamma \mathcal{R} T_0}}. \tag{89}$$

For $Ma \geqslant 1$, therefore, we would expect the modified boundary condition to recover the standard LODI assumption, which, in agreement with the $Ma = 1.1$ test-case presented by Poinsot and Lele [12], produces negligible flow distortion and no acoustic waves re-entering the domain as the flow regime is supersonic.

When the flow is subsonic, standard NSCBC is still able to prevent fairly well distortion of vorticity isolines when the vortex leaves the domain; this is true for $Ma = 0.575$ and $Ma = 0.863$ but not for very low Mach number flows (see Fig. 1(a)), as already shown by Prosser [14], where vorticity contours undergo significant distortion at the boundary. Furthermore, the standard non-reflecting boundary produces significant distortion of the longitudinal velocity and Q contours: also in this case, the effect is more and more pronounced when reducing the Mach number but it seems that these quantities are slightly more affected (the flow tends to align orthogonally to the boundary and a disturbance in the strain is produced). On the other hand, the pressure field shows a somehow opposed behavior: boundary generated pressure noise amplitude becomes more and more important when increasing the Mach number but, obviously, also less and less able to re-enter the domain. For the $Ma = 0.575$ test, a pressure perturbation with a total amplitude that is about 43 times higher than the initial vortex pressure drop is observed at the boundary (see Fig. 2(a)). Nonetheless, even at low Mach, the pressure field is significantly distorted as shown in Fig. 4(a).

The proposed 3D-NSCBC produces almost no distortion in vorticity, longitudinal velocity and Q contours meaning that vorticity is well conserved and no additional strain is generated at the boundary for all the Mach numbers (Figs. 1–3(b–d–f)). Furthermore, the pressure field distortion is dramatically reduced and the pressure perturbation amplitude is reduced of about a factor 6, 214 and 60 for the low, mid and high Mach test-cases, respectively. Pressure contours for the low Mach number case are shown in Fig. 4(b) where the expected profiles—concentric circles—are quite well reproduced.

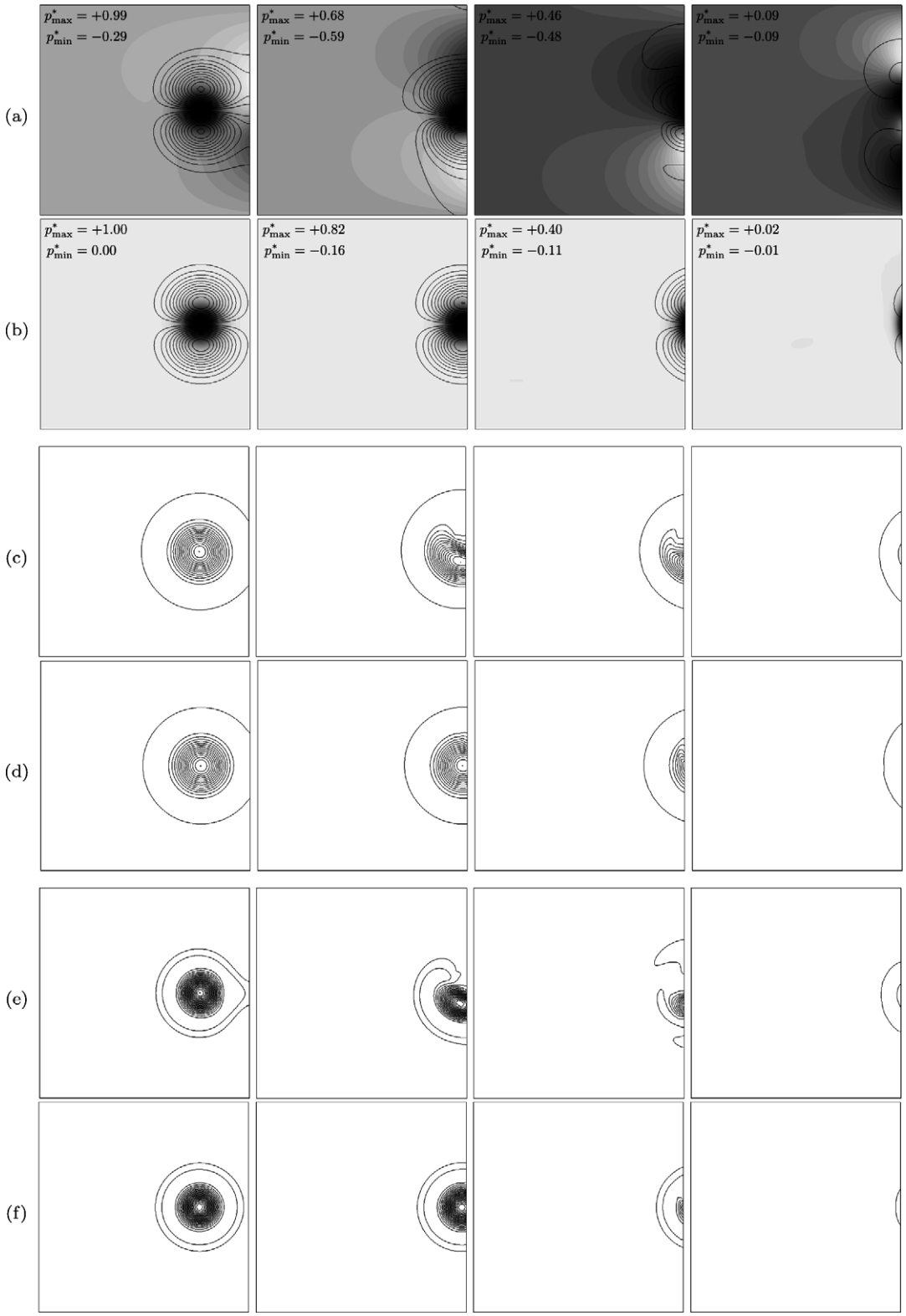

Fig. 1. Vortex test: $Ma = 0.00575$. Standard NSCBC (a–c–e) and 3D-NSCBC (b–d–f). Normalized pressure field (see Eq. (88)) and longitudinal velocity contours (a, b); vorticity contours (c, d); Q contours (e, f). Frames at increasing time from left to right.

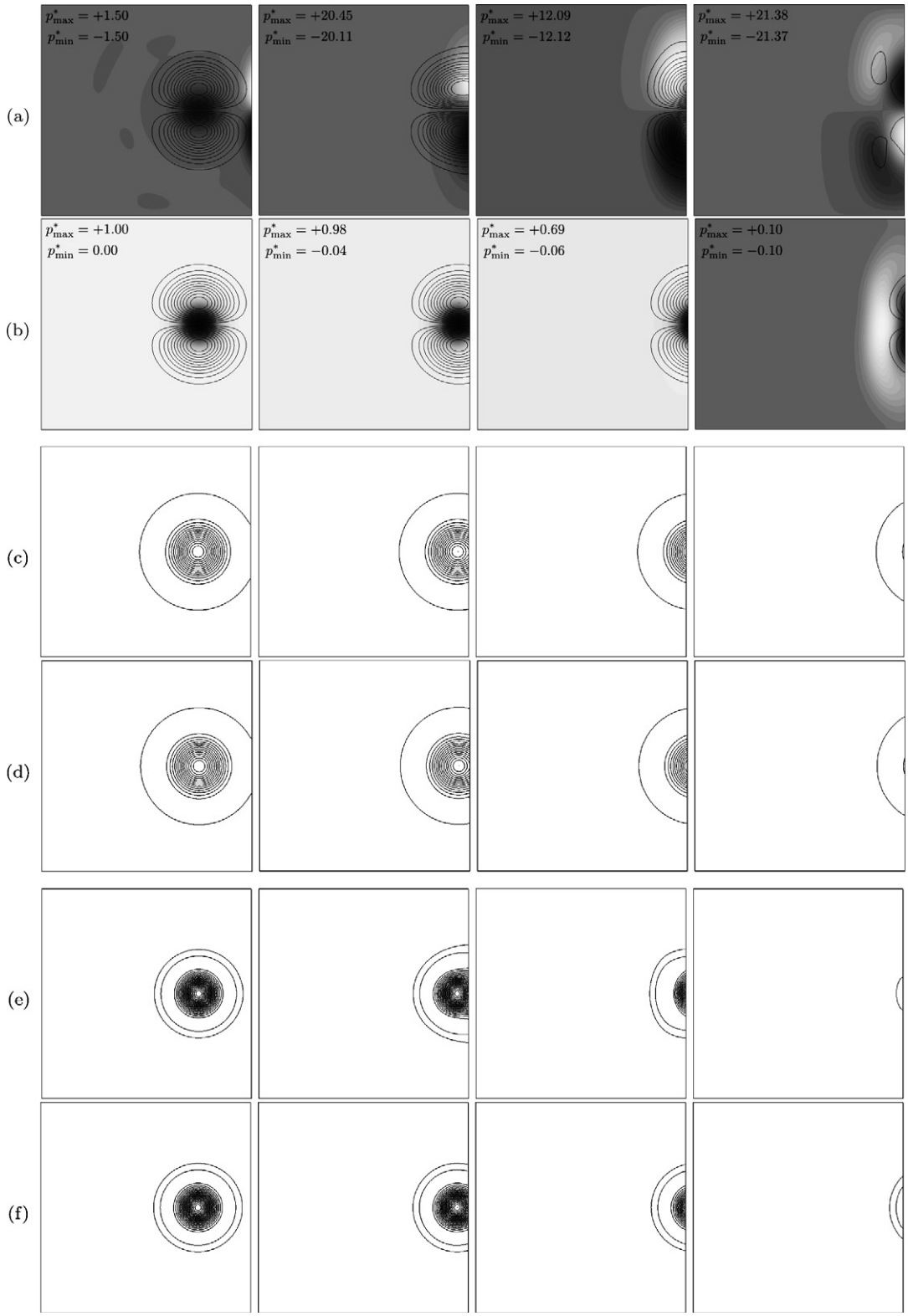

Fig. 2. Vortex test: $Ma = 0.575$. Standard NSCBC (a–c–e) and 3D-NSCBC (b–d–f). Normalized pressure field (see Eq. (88)) and longitudinal velocity contours (a, b); vorticity contours (c, d); Q contours (e, f). Frames at increasing time from left to right.

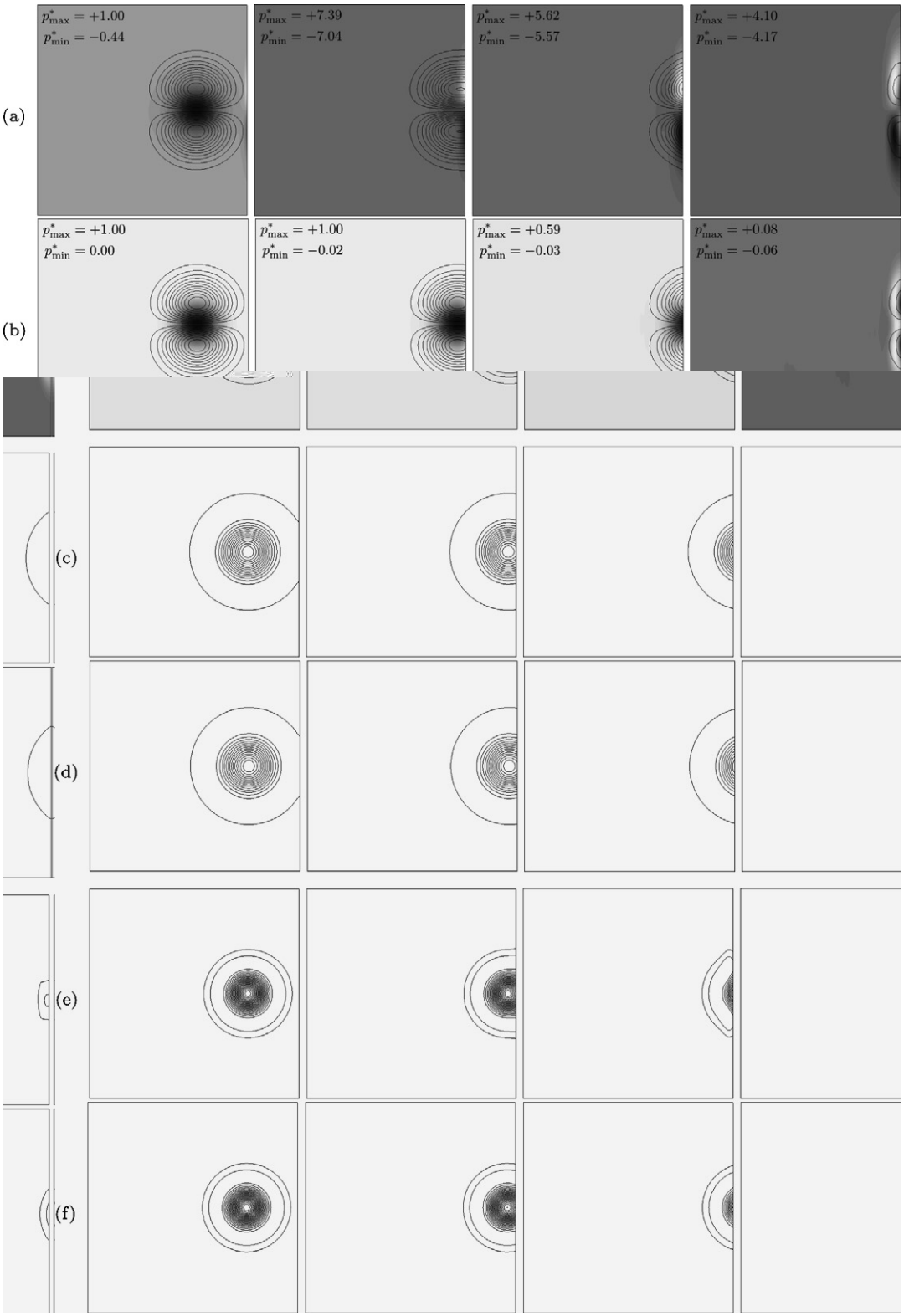

Fig. 3. Vortex test: $Ma = 0.863$. Standard NSCBC (a–c–e) and 3D-NSCBC (b–d–f). Normalized pressure field (see Eq. (88)) and longitudinal velocity contours (a, b); vorticity contours (c, d); Q contours (e, f). Frames at increasing time from left to right.

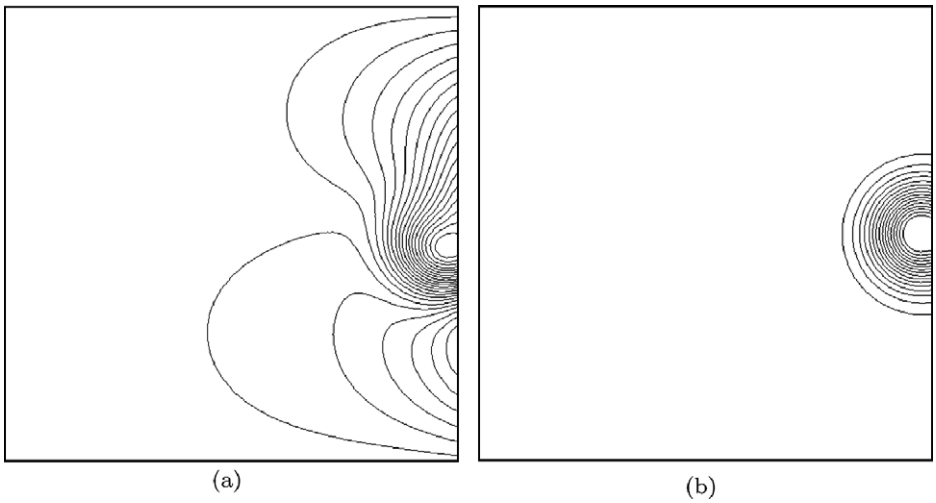

Fig. 4. Vortex test: pressure contours as the vortex crosses the boundary ($Ma = 0.00575$). Standard NSCBC non-reflecting outflow (a); 3D-NSCBC non-reflecting outflow (b).

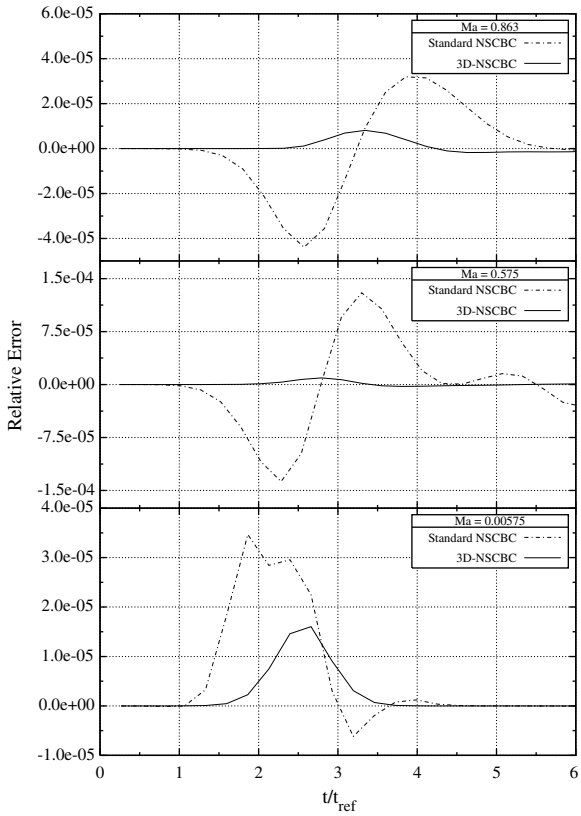

Fig. 5. Vortex test: time evolution of the relative error in pressure with respect to the benchmark solution on the extended domain. Sampling point is located at the boundary, on the vortex centerline; $t_{\text{ref}} = L/(5U_0)$.

Fig. 5 shows, for the three test-cases, the error on the computed centerline boundary pressure (at $x_1 = L/2$ and $x_2 = 0$) relative to a benchmark solution computed over an extended domain of length $2L$:

$$\varepsilon_r(\boldsymbol{x},t) = \frac{p(\boldsymbol{x},t) - p^0(\boldsymbol{x},t)}{p^0(\boldsymbol{x},t)}, \tag{90}$$

where $\boldsymbol{x}$ denotes the sampling location and p^0 is the pressure computed on the benchmark simulation.

As expected, the improvement with the modified boundary condition is more evident at higher Mach numbers where the amplitude of the pressure disturbance generated using the LODI non-reflecting outflow is higher; in these cases, using the modified approach, the spurious pressure wave is almost completely avoided and the computed solution follows quite well the benchmark solution. Even at low Mach, the new proposed method reduces the error of about a factor 2. In any case, the novel approach avoids any oscillatory behavior: the relative error is always positive during all the vortex transition event, meaning that the pressure drop at the vortex core is slightly under-predicted when the vortex reaches the boundary.

4.2. Single vortex with flow inversion

Another two-dimensional vortex test is presented in this section. The vortex strength C_v has now been increased in order to produce a relatively strong reversed flow at the outflow. This is a particularly stringent test for non-reflecting boundary conditions, as the reversed flow requires the specification of additional information, coming from the outside of the computational domain, which is hard to be prescribed a priori.

For the present test, $C_v = 3 \times 10^{-1}$ m^2/s, R_v was set at 10% of the domain size L, $p_\infty = 1$ atm, $T_0 = 300$ K and the convective velocity U_0 was set at 100 m/s ($Ma = 0.286$ and $Re = \rho U_0 R_v/\mu \simeq 8300$). The relaxation parameter for pressure σ was set at 0.28 and the transverse relaxation parameter $\beta = 0.286$ ($\mathbb{T}^1_{1,\mathrm{ex}} = 0$).

The value of C_v is now high enough to create a region of reversed flow, as it can be observed in the initial velocity profile in Fig. 6, where horizontal velocity attains a negative peak of about 40 m/s for $0.0007 < x_2 < 0.002$. In those parts of the outflow boundary where reversed flow is created, the standard perfectly non-reflecting procedure is applied and all the entering waves traveling with convective velocity u_1—namely, $\mathcal{L}_2$, $\mathcal{L}_3$, $\mathcal{L}_4$ and $\mathcal{L}_6$—are set to zero.

Fig. 7 shows the behavior of the 3D-NSCBC technique compared to the standard NSCBC in terms of pressure error; as in the previous section, the error has been estimated over a benchmark solution computed on an extended computational domain (two times longer). The top plot shows a normalized global error measure defined as

$$\varepsilon(t) = \frac{\left[\sum_{i,j,k}\left(p_{i,j,k}(t) - p^0_{i,j,k}(t)\right)^2\right]^{1/2}}{\left[\sum_{i,j,k}\left(p^0_{i,j,k}(t)\right)^2\right]^{1/2}}, \tag{91}$$

where the i,j,k subscript refers to the grid location and p^0 is the pressure computed on the benchmark simulation. The bottom plot shows the relative error measured on a point located at the outflow boundary on the vortex centerline (see Eq. (90)).

Fig. 8 shows the normalized global error in vorticity, which is defined in analogy with Eq. (91) as

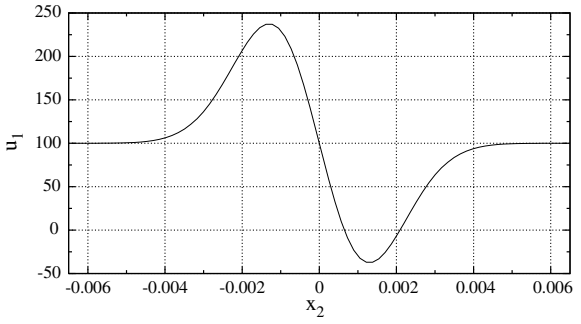

Fig. 6. Vortex test with flow reversal: initial u_1 velocity profile along a vertical plane passing through the vortex center.

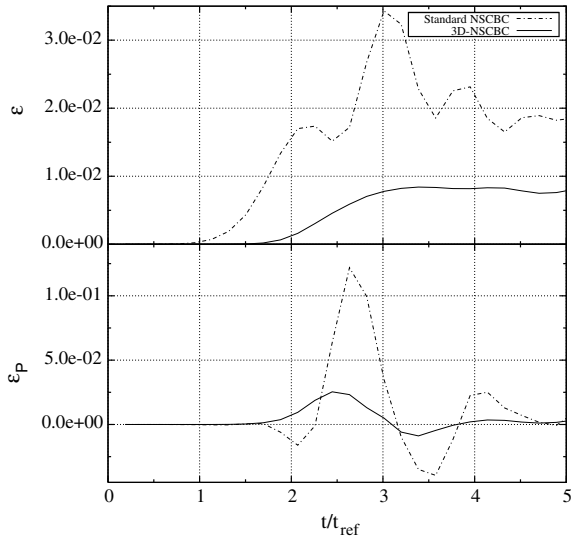

Fig. 7. Vortex test with flow reversal: time evolution of the pressure error. Global normalized error (top); relative error (bottom) for a point located at the boundary, on the vortex centerline; $t_{\mathrm{ref}} = L/(5U_0)$.

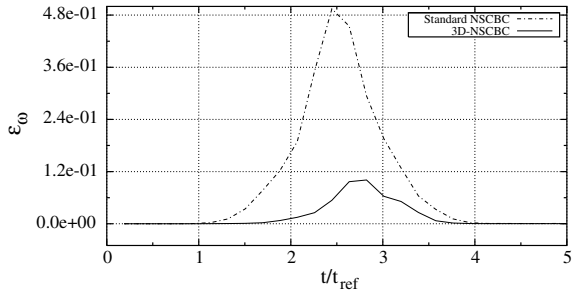

Fig. 8. Vortex test with flow reversal: time evolution of vorticity normalized error; $t_{\mathrm{ref}} = L/(5U_0)$.

$$\varepsilon_\omega(t) = \frac{\left[\sum_{i,j,k}(\omega_{i,j,k}(t) - \omega^0_{i,j,k}(t))^2\right]^{1/2}}{\left[\sum_{i,j,k}(\omega^0_{i,j,k}(0))^2\right]^{1/2}}. \tag{92}$$

Even when the vortex strength is enough to create flow inversion at the outflow, a certain improvement is observed over the standard NSCBC approach, when using the 3D-NSCBC technique. In terms of normalized global measures, pressure error is reduced by a factor of about 2; with regards to the vorticity, the error peak is more than four times less than in the simulation performed with standard mono-dimensional boundary conditions. This is not surprising, as the 3D-NSCBC approach is expected to get advantage by the inclusion of transverse effects, therefore allowing a correct propagation of vorticity across the boundary.

4.3. Vortex dipole

In this section a test is presented concerning a convected dipole of co-rotating vortices. This problem is characterized by a certain level of unsteadiness as the two vortices slowly rotate around each other. The flow field is initialized with the following stream function [14]:

$$\Psi = C_v\left[\exp\left(-\frac{r_1^2}{2R_v^2}\right) + \exp\left(-\frac{r_2^2}{2R_v^2}\right)\right] + U_0 x_2 \tag{93}$$

with

$$r_1 = \sqrt{x_1^2 + (x_2 + \delta)^2}, \tag{94}$$

$$r_2 = \sqrt{x_1^2 + (x_2 - \delta)^2}. \tag{95}$$

The vortex strength C_v was equal to 1.25×10^{-3} m^2/s, R_v and δ were set at 10% and 15% of the transverse domain size L, respectively and the free-stream velocity U_0 was set at 0.5 m/s (Ma=0.00144 and $Re = \rho U_0 R_v/\mu \simeq 42$). The relaxation parameter for pressure σ and the transverse relaxation parameter β were 0.28 and 0.00144, respectively ($\mathbb{T}^1_{1,\mathrm{ex}} = 0$).

Again in this case we performed a reference simulation over a longer domain of length $2L$ in order to have a benchmark solution to compare with. The relevant results, in terms of pressure (Eqs. (90) and (91)) and vorticity (Eq. (92)) errors are shown in Figs. 9 and 10, respectively. Local relative error, in particular, has been sampled at the boundary on two points, P1 and P2, corresponding approximately to the upper and lower vortex centers, respectively.

Results, both in terms of pressure and vorticity errors, are generally in line with those presented in the previous sections. It should be noted that, due to the slow rotation of the two vortices around each other, the lower and the upper vortex's centers cross the outflow boundary at different times, namely $t/t_{\mathrm{ref}} \simeq 2.1$ and $t/t_{\mathrm{ref}} \simeq 3.2$, respectively (as it was inferred observing the pressure field computed on the benchmark solution). As the maximum normalized pressure error is, in general, attained at the moment the vortex core leave the domain, the two peaks in the global normalized error curve (Fig. 9 on top) indicate precisely those two moments. Interestingly, the standard NSCBC boundary produces a shift to the left of the peaks: the pressure field is perturbed in such a way that the two vortices seem to leave the domain earlier than expected. On the

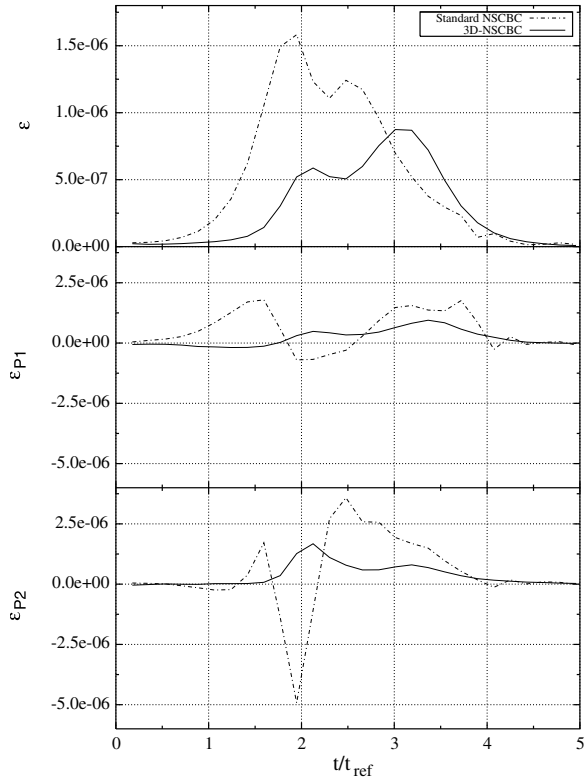

Fig. 9. Vortex dipole test: time evolution of the pressure error. Global normalized error (top); relative error for a point located at the boundary, on the upper vortex centerline (middle); relative error for a point located at the boundary, on the lower vortex centerline (bottom); $t_{\mathrm{ref}} = L/(5U_0)$.

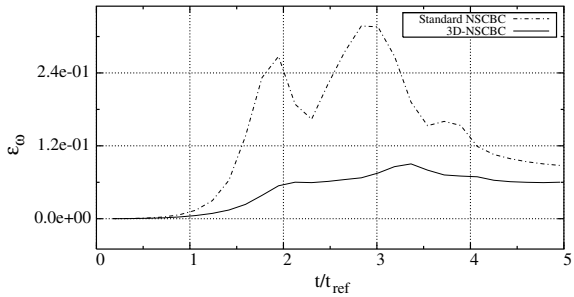

Fig. 10. Vortex dipole test: time evolution of vorticity normalized error; $t_{ref} = L/(5U_0)$.

other hand, no shift is observed in the error curve relevant to the simulation performed using the 3D-NSCBC outflow.

Again, the most evident improvement is obtained in terms of vorticity, the relevant normalized global error is about three times lower when using the 3D-NSCBC technique.

Fig. 11 shows the normalized pressure p^* (see Eq. (88)) and the iso-contours of the longitudinal velocity u_1 at three consecutive instants in time. The benchmark solution over the first half of its computational domain is depicted on top (Fig. 11(a)), the solution computed using the 3D-NSCBC approach in the middle (Fig. 11(b)) and the solution computed using the standard NSCBC at the bottom (Fig. 11(c)). The frames have been chosen to show the moment the lower vortex leaves the domain. The 3D-NSCBC is still able to allow a fairly good reproduction of the expected solution, both in terms of pressure map and velocity field. On the other hand, the

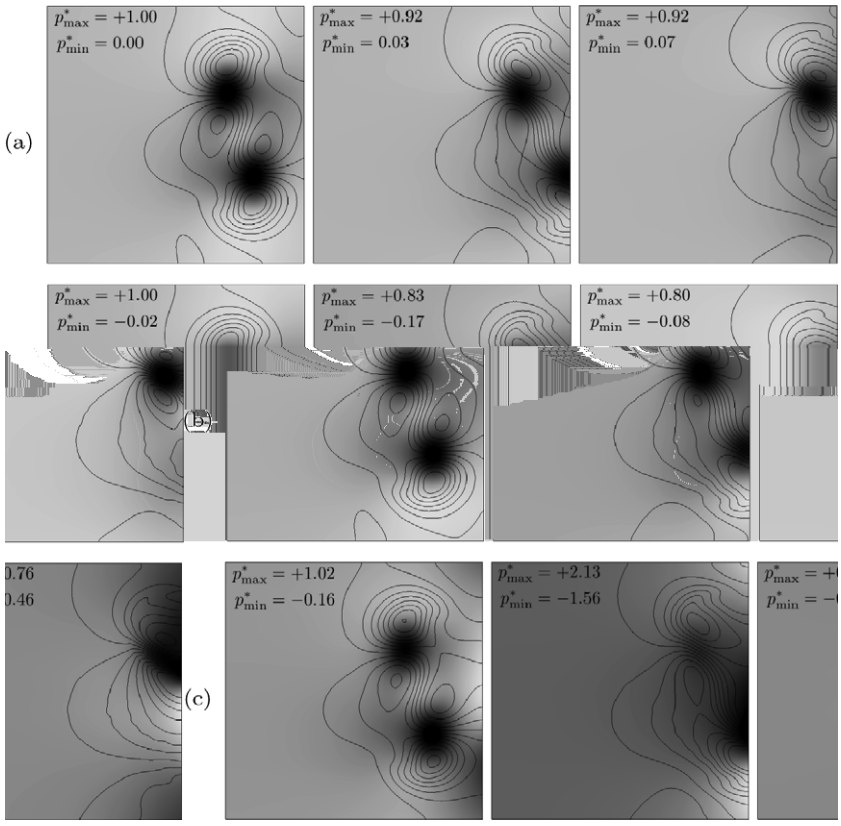

Fig. 11. Vortex dipole test. Benchmark solution on first half of domain (a), 3D-NSCBC (b) and Standard NSCBC (c) on full domain. Normalized pressure field (see Eq. (88)) color map and longitudinal velocity contours. Frames at increasing time from left to right.

standard NSCBC produces a strong perturbation to the pressure field—a pressure perturbation with a total amplitude of about 370% the initial pressure drop is observed in the second frame of Fig. 11(b)—and the vector field becomes quite distorted, especially after the lower vortex has left the domain.

4.4. Spherical pressure wave

The fourth test-case is a tridimensional flow configuration designed to assess the behavior of the proposed approach for edges and corners. The computational domain is a cube of side $L = 0.013$ m with non-reflecting outflows on all the six faces, Outflow/outflow edge conditions on all the 12 edges and Outflow/outflow/outflow corner conditions on all the eight corners.

The pressure field was initialized with a spherical pressure pulse of amplitude δ:

$$p(r) = p_\infty \left[1 + \delta \exp\left(-\frac{r^2}{2R_p^2} \right) \right], \tag{96}$$

where $r = \sqrt{x_1^2 + x_2^2 + x_3^2}$ is the distance from the center of the computational domain and R_p is the characteristic dimension of the pressure pulse. Assuming that the temperature is constant and equal to T_0, the initial density distribution can be computed from the state equation: $\rho(r) = p(r)/(\mathcal{R}T_0)$.

For the present test, δ was set at 0.001, R_p was set at 5% of the domain size L, $p_\infty = 1$ atm, and $T_0 = 300$ K. The flow field was initialized at rest and then left to evolve in order to compare the evolution of the spherical pressure wave front—especially when approaching the computational domain edges and corners—when using standard NSCBC and 3D-NSCBC approach.

As in the previous test, the computation was done setting $\mathbb{T}^*_{k,\mathrm{ex}} = 0$ (superscript $*$ equal to 1 or 5 depending on the outflow's location and $k = 1, 2, 3$) over all the outflows, as the steady state is expected to be characterized by uniform pressure and zero velocity. With regards to the transverse damping parameter β, considering what has been observed in the vortex test-case, it seemed reasonable to use a value somehow related to a typical Mach number for this particular flow. A possible choice is then the maximum Mach number relevant to the local fluid displacement produced by the acoustic wave. As it will be shown, this simple approach gives fairly good results. On the other hand, some tests carried out varying β have given an optimal value of about 0.5, which is 4 order of magnitude higher than the mentioned Mach number. We report in what follows the results from three tests which have been made changing both the transverse relaxation coefficient and the pressure relaxation coefficient: $\beta = Ma_{\max}$ and $\sigma = 0.28$; $\beta = Ma_{\max}$ and $\sigma = 3.00$; $\beta = 0.5$ and $\sigma = 0.28$.

Qualitative results in terms of pressure field have been extracted over the two cutting planes P1 and P2 depicted in Fig. 12. These planes were chosen to assess the pressure field distortion on corners and edges, respectively.

With regards to test T3, Fig. 13 shows the pressure field and pressure contours, at two slightly different timesteps, when the pressure wave fronts are well cut by the domain boundaries. As expected, the LODI assumption (standard NSCBC) is too restrictive for such a tridimensional flow and the introduction of transverse effects at the boundary helps in reducing flow distortion, especially in regions where the flow field is not perpendicular to the outlet (i.e. toward edges and corners). The 3D-NSCBC technique, instead, is able to preserve pressure wave front curvature, whereas the standard non-reflecting outflow shows a tendency to reduce curvature or even to reverse it (see, for instance, pressure contours at the top left corner of Fig. 13(c)). The level of numerical reflection is significantly reduced too, as it can be observed in the region just behind the pressure wave. The results from tests T1 and T2 (not shown) are slightly worse but still better than those obtained with the LODI assumption. Moreover, no significant difference has been observed when increasing σ, meaning that the modified NSCBC allow a certain freedom in the choice of the pressure relaxation coefficient.

It should be noted that the present configuration is a particularly tough test-case for both NSCBC and 3D-NSCBC non-reflecting outflows. The pressure wave, as expected, is accompanied by two opposed local displacements of equal amplitude, as it is shown in Fig. 14, where the velocity field is superimposed to the pressure map. The presence of local back-flow regions at the outlet poses the additional problem about how incoming characteristic waves traveling with the convective velocity (i.e. characteristic waves with indices 2, 3, 4 and 6) should be imposed. Previous tests have shown that just "ignoring" the possibility of a reversed flow

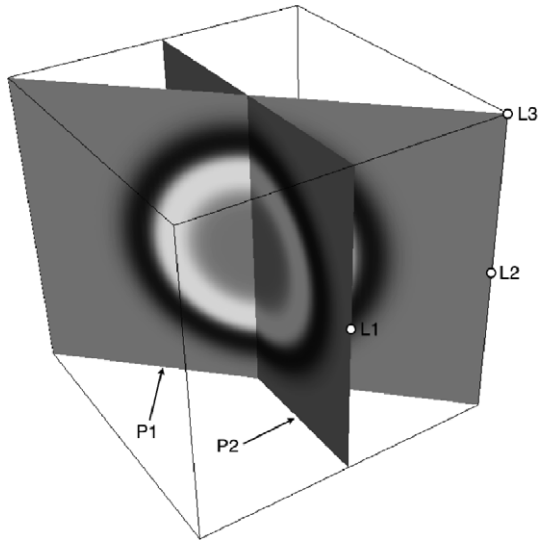

Fig. 12. Spherical pressure wave test: position of the cutting planes P1 and P2 and of the sampling locations L1, L2 and L3.

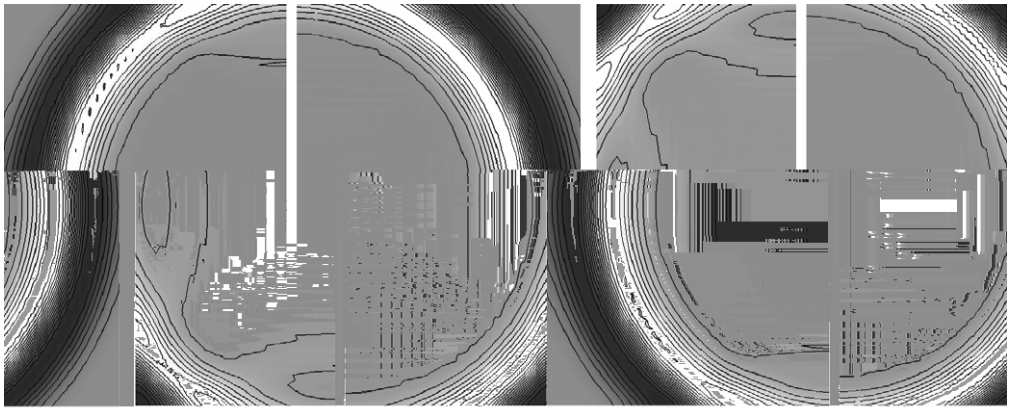

Fig. 13. Spherical pressure wave test T3: pressure map and pressure contours on plane P1 (a,b) and P2 (c,d). Standard NSCBC non-reflecting outflows (a, c); 3D-NSCBC non-reflecting outflows (b, d).

event and keep computing the relevant characteristic wave amplitudes using interior points may lead to instability problems, especially when the back-flow is particularly persistent in time. An efficient solution is to set these convected incoming waves to zero in regions of local back-flow. The drawback of this simplistic approach is, of course, a slight reduction of boundary transparency.

A measure of the error has been extracted using a benchmark solution computed on a two times wider domain. Three different locations on the boundary (see Fig. 12) have been taken into account: boundary face center (L1), boundary edge center (L2) and boundary corner (L3). The local relative absolute error on pressure for these points has been measured as

$$\varepsilon_r(\boldsymbol{x},t) = \frac{|p(\boldsymbol{x},t) - p^0(\boldsymbol{x},t)|}{p^0(\boldsymbol{x},t)}, \tag{97}$$

where $\boldsymbol{x}$ denotes the sampling location and p^0 is the pressure computed on the reference simulation. Furthermore, the overall performance of the 3D-NSCBC approach has been quantified resorting to the normalized error measure defined in Eq. (91).

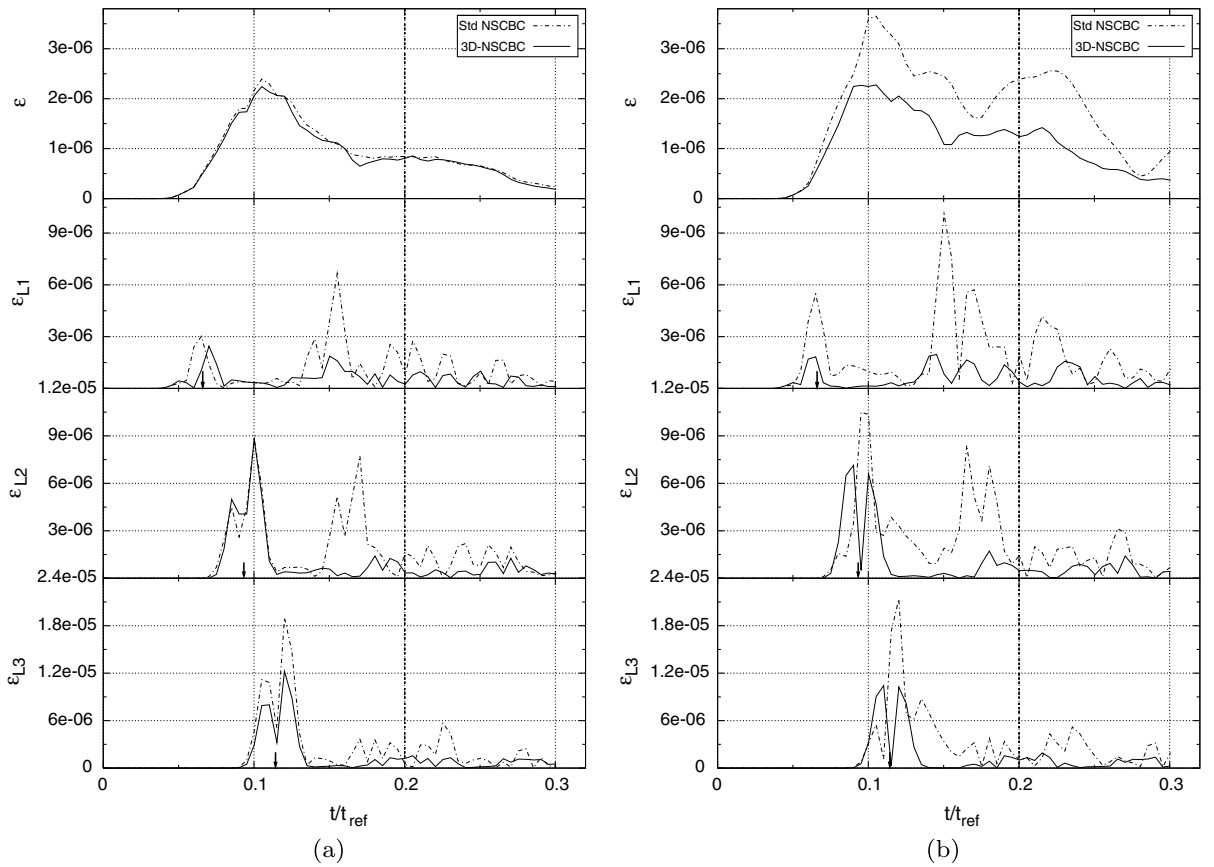

Fig. 15. Spherical pressure wave test: normalized error on pressure for test-case T1 (a) and test-case T2 (b). Global normalized error on the top graph (see Eq. (91)) and local relative error at boundary locations L1, L2 and L3. The vertical arrows mark the instants when the pressure pulse crosses locations L1, L2 and L3, respectively ($t_{ref} = 2.8 \times 10$

Figs. 15 and 16 show the relevant results. It should be noted that for $t/t_{ref} \simeq 0.2$ the reference solution (bigger domain) is expected to become more and more affected by its own boundary and the comparison becomes meaningless: this is marked by a vertical dashed line limiting the region of interest.

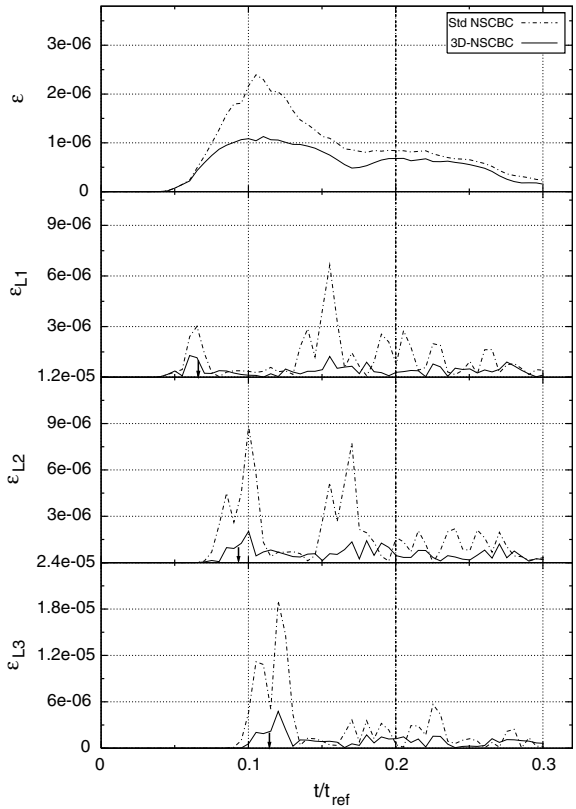

Fig. 16. Spherical pressure wave test: normalized error on pressure for test-case T3. Global normalized error on the top graph (see Eq. (91)) and local relative error at boundary locations L1, L2 and L3. The vertical arrows mark the instants when the pressure pulse crosses locations L1, L2 and L3, respectively ($t_{\text{ref}} = 2.8 \times 10^{-4}$ s).

In general, the maximum error—as per Eq. (91)—occurs, of course, during the period when the boundaries are crossed by the pressure pulse. With regards to tests T1 (low relaxation) the error level is less than about 0.14% and no significant improvement is observed using 3D-NSCBC approach. On the other hand, when the relaxation coefficient is increased (T2), the simulation performed resorting to NSCBC hypothesis is characterized by a higher error, meaning that the boundary conditions are less transparent and numerical reflected pressure waves have higher amplitude. The 3D-NSCBC, on the other hand, maintains the error almost unchanged, and the level of boundary reflection is only slightly increased.

In terms of local relative error, the novel approach gives, in general, more accurate results, showing a favorable tendency to produce numerical reflected waves of small amplitude; also in this case, when increasing σ, the LODI approximation (standard NSCBC) produces higher reflection, whereas the modified approach remains significantly more transparent, the level of boundary reflection being marginally affected by the pressure relaxation coefficient σ.

Test-case T3 gives the better performance (see Fig. 16). In this particular case, the normalized maximum error is reduced of about a factor 2 and the local relative error is significantly reduced even when the pressure pulse crosses the critical locations L2 and L3.

Fig. 17 shows a comparison about the evolution of the pressure wave. The pressure wave was looked at different time-steps before it had reached the boundary and radial plots were extracted at each time-step (symbols). As expected for a spherical wave, the pulse amplitude decreases continuously as the wave front expands. Regarding the pressure pulse as a signal traveling with the speed of sound c, the time evolution of pressure can be rescaled as a radial plot using the following equivalence relation between space and time for such a wave:

$$f(r - ct_0) \equiv f(r_0 - ct) \quad \text{with } ct_0 = r_0, \tag{98}$$

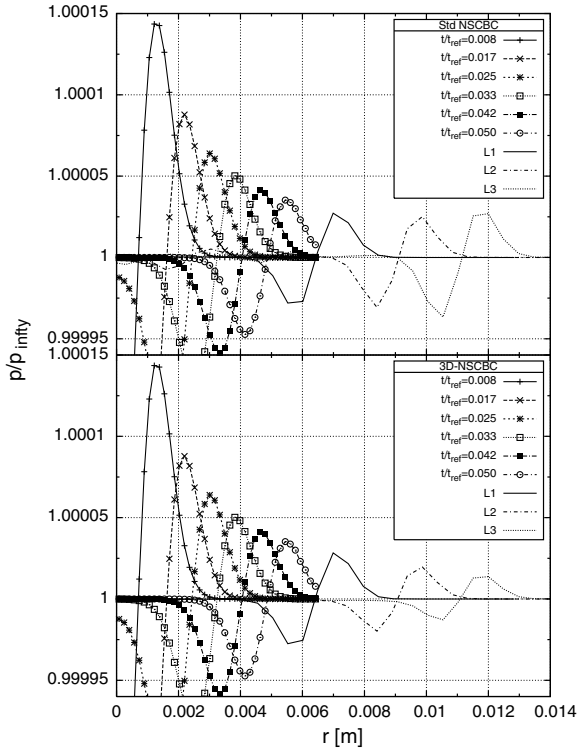

Fig. 17. Spherical pressure wave test: normalized pressure wave evolution for test-case T3. Symbols are radial pressure plots at different normalized time-steps ($t_{\text{ref}} = 2.8 \times 10^{-4}$ s); lines are temporal pressure plots at locations L1, L2 and L3 rescaled as radial plots under the assumption that the pressure pulse is a signal traveling with speed $c \simeq 347.6$ m/s.

$$\Rightarrow r - r_0 = r_0 - ct \tag{99}$$

with $c \simeq 347.6$ m/s and r_0 the radial distance of the time signal's sampling location.

Once the pressure front meets the boundary, the LODI assumption is unable to retain the correct physical information about the tridimensionality of the flow: the pressure front stops behaving as a spherical wave and reaches the edge and, later on, the corner retaining almost the same amplitude. On the other hand, the 3D-NSCBC outflow and the proposed edge/corner technique, is remarkably capable of preserving the correct physical information and the pressure front reaches the boundary edges and corners with the expected reduced amplitude.

Finally, a qualitative comparison of the computed wave front at three subsequent time-steps is shown in Fig. 18. The wave front is shown by means of pressure iso-surfaces relevant to a normalized pressure value of 1000.98 ($p_{\text{ref}} = 101.23$ Pa) and is expected to be perfectly spherical; results are relevant to the test-case T3. The innermost and the outermost surfaces have been chosen in order to "enclose" the pressure pulse. Spurious numerical reflection is expected to be generated starting from the moment the outermost surface crosses the boundary; the effects are then visible on what follows, namely, the innermost surface. As it can be observed, the 3D-NSCBC outflows allow the wave front curvature to be correctly preserved. Negligible reflection is produced and the wave front undergoes minimal distortion even when the pressure pulse is well outside the computational domain (Fig. 18(c)). On the contrary, the computation performed resorting to the LODI assumption is characterized by significant distortion of the core pressure field; even the outermost surface itself is progressively deformed with local regions where the curvature is reversed (see Fig. 18(e) and (f)).

4.5. Jet flow configurations

We have analyzed some basic test-cases on simple configurations so far, in order to assess the behavior of the 3D-NSCBC non-reflecting outflows when compared to the standard LODI (NSCBC) assumption. In this

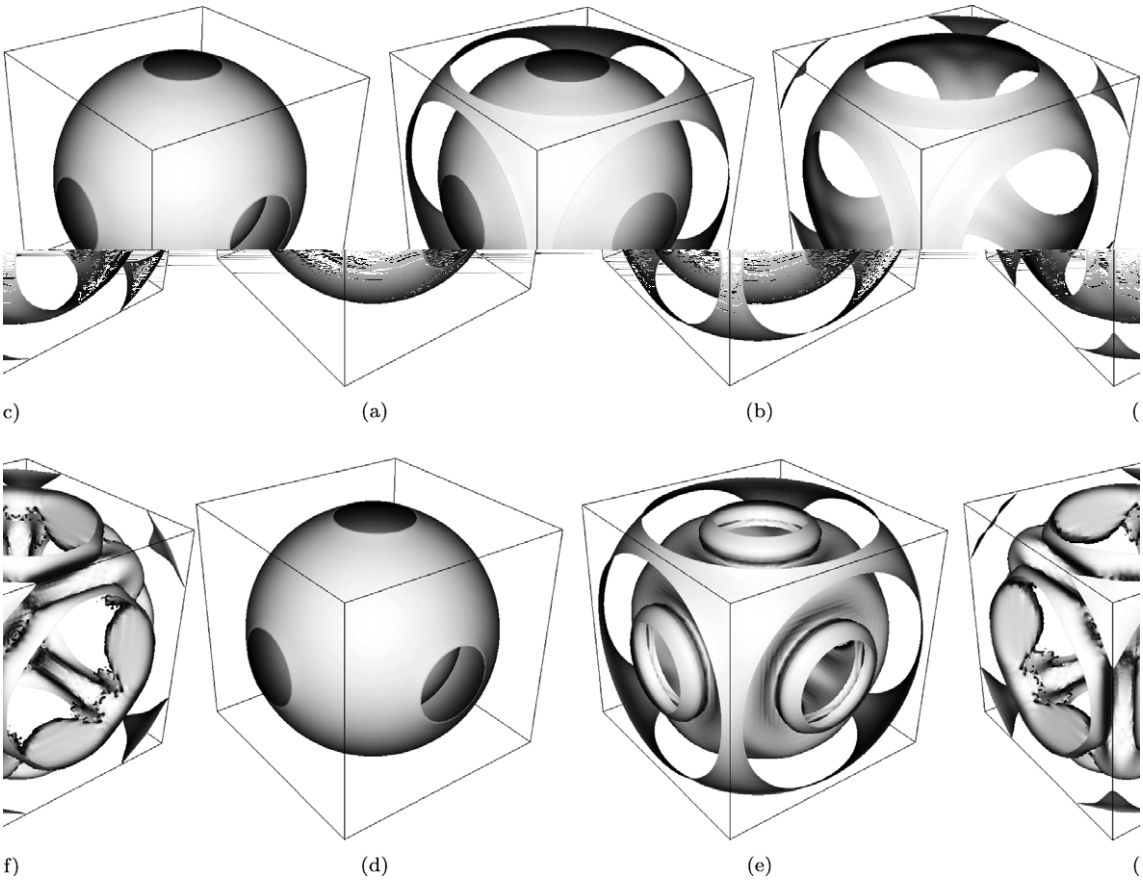

Fig. 18. Spherical pressure wave test (T3): pressure iso-surfaces evolution (iso-value $p/p_{\text{ref}} = 1000.98$). 3D-NSCBC non-reflecting outflows (a–c), standard NSCBC non-reflecting outflows (d–f).

section we present qualitative results from two simulation of more complex geometries: (a) LES of compressible turbulent free round-jet and (b) LES of compressible turbulent impinging round-jet.

Though only qualitative, as already said, these test were chosen to apply the novel approach on configurations involving non-reflecting inlet/outlet coupling, as well as all the types of edge/corner conditions presented in the precedent sections.

As just mentioned, both the simulation were performed in turbulent regime resorting to the LES technique. Within the framework of LES approach, the Navier–Stokes equations are filtered with a low-pass filter, the low-frequency components of the flow field—those which represent the large scale structures of the flow—being directly resolved, and the coupling term arising from the non-linear convective term being modeled by the sub-grid scale (SGS) model. We adopt an implicit filtering approach, therefore, the filter's cutoff length Δ is equal to the local grid spacing, while SGS terms are modeled using the eddy viscosity assumption of the wall-adapting local eddy-viscosity model proposed by Nicoud and Ducros [10].

4.5.1. Turbulent free round-jet

The computational domain is a box of dimensions $14D \times 5D \times 5D$ with $D = 0.0026$ m the jet diameter ($200 \times 80 \times 80$ grid points). The grid is uniform along x_1 and slightly stretched along x_2 and x_3 in order to better resolve the jet shear layer; transverse refinement was limited to maintain a maximum stretching ratio of about 1.06 over consecutive cells. The resulting grid spacing is: $\Delta x_t/D \simeq 0.0527$ on the axis, $\Delta x_t/D \simeq 0.0431$ at $x_t = \pm D/2$ and $\Delta x_t/D \simeq 0.1312$ at $x_t = \pm 2.5D$ $(t = 2, 3)$.

The inflow is located at $x_1 = 0$ and the modified subsonic non-reflecting inflow is used, with the velocity relaxation parameter η_5 set at 3.58. The same value was set for the other inlet relaxation parameters:

$\eta_2 = -3.58$ and $\eta_3 = \eta_4 = \eta_6 = 3.58$. The target inlet velocity was imposed using the power law profile for turbulent pipe flow:

$$\frac{U(r)}{U_{\mathrm{cl}}} = \left(1 - \frac{2r}{D}\right)^{1/n}, \tag{100}$$

where $r = \sqrt{x_2^2 + x_3^2}$ is the distance from the jet axis, U_{cl} is the centerline velocity and the parameter n was set at 7.4; the ratio between bulk velocity U_{b} and centerline velocity U_{cl} is about 0.82. The value of U_{b} was computed fixing the value of the jet's Reynolds number: $Re_D = \rho U_{\mathrm{b}} D/\mu = 23,000$. A correlated random noise [8] was superimposed to the velocity profile with an intensity of 0.8% of the bulk velocity U_{b}. The inlet temperature was fixed at 300 K.

All the other boundaries are non-reflecting outflows with pressure relaxation parameter σ set at 0.28 and target pressure equal to 1 atm. The assumed exact transverse terms were set at zero, which seemed a reasonable approach in consideration of the results obtained in the previous tests. The transverse relaxation parameter β was set at 0.19, a typical value of the Mach number for this specific flow, as it has been evaluated from a precursor simulation performed with β equal to U_{b}/c. Inflow/outflow edge conditions are used on the four bottom edges and Inflow/outflow/outflow corner conditions are used on the relevant four joining corners; Outflow/outflow edge conditions are used on the eight remaining edges and Outflow/Outflow/Outflow corner conditions on the four top corners (see Fig. 19). The simulation was started from fluid at rest and at reference condition (1 atm, 300 K) all over the domain.

The developed flow field is depicted in Fig. 19, where the coherent vortical structures are represented resorting to the Q criterion. Pressure and passive scalar distributions over axial planes are shown too. Despite the fairly small computational domain used, no perturbation coming from the boundaries is observed: the

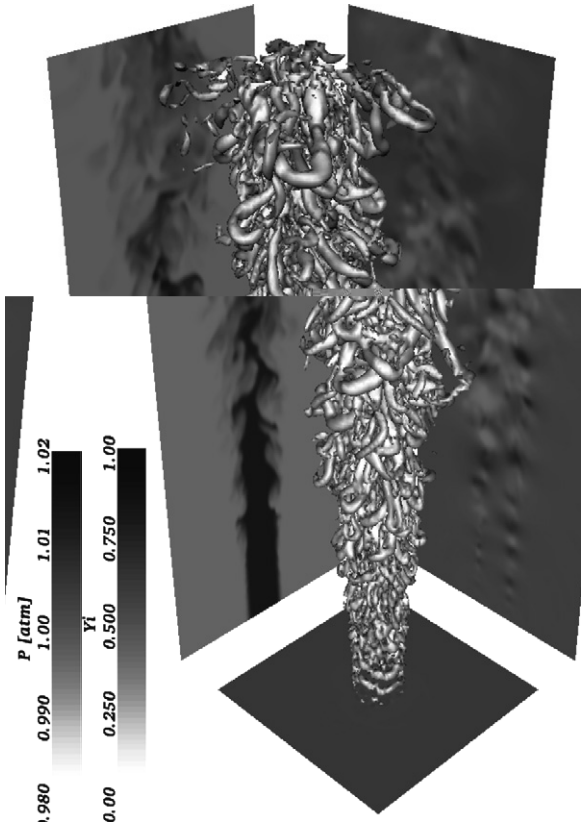

Fig. 19. Free round-jet with 3D-NSCBC: $Q = 0.5$ contours (center), passive scalar (left) and pressure (right) distributions over orthogonal axial planes ($t = 157.1D/U_{\mathrm{b}}$).

pressure field reflects the presence of vortical structures and is smooth and on the target values in regions not affected by the flow. The compatibility conditions for inlet/outlet edges and corners allow perfect transition from the inlet to the outflow boundaries without producing any "square-shaped" pressure pattern. The complex of vortical structures which develops along the jet, is able to leaves the domain through the outflows without being significantly perturbed (see Fig. 20).

On the other hand, the same simulation performed using the standard NSCBC approach—see Fig. 21—underwent a destabilization of the pressure, originating on an outflow's corner with a peak of low pressure; this destabilization caused the jet to collapse toward the low pressure region as it can be observed in the figure. Moreover, the inlet side is far more noisy and a chessboard pattern is visible on the pressure map over the inlet plane. Looking at the vortical structures, turbulent structures seem a bit less developed, especially at the beginning of the jet. The problem is clearly linked to the observed inlet pressure noise (see axial pressure map on the right of Fig. 21), which interacts with the shear layer development and prevents the appearance of Kelvin–Helmholtz-type instabilities up to a distance of about one diameter from the jet's nozzle.

From the above results, it is clear that such a simulation is not feasible with standard NSCBC unless: (a) a greater value of the pressure relaxation coefficient σ is used in order to better control the pressure at the boundary (thus leading to higher reflection); (b) a wider computational domain is used in order to prevent the jet from *falling* into a lateral outflow. This notwithstanding, the inlet noise could remain an issue.

4.5.2. Turbulent impinging round-jet

For this last test-case, the computational domain is a box of dimensions $2D \times 7D \times 7D$ with $D = 0.0026$ m the jet diameter ($90 \times 146 \times 146$ grid points). The grid is refined along x_1 in the near-wall region and slightly stretched along x_2 and x_3 in order to better resolve the jet shear layer; refinements in the three directions were limited to maintain a maximum stretching ratio of about 1.04 over consecutive cells. The resulting grid spacing along x_1 is: $\Delta x_1/D \simeq 0.0443$ at the jet's nozzle exit and $\Delta x_1/D \simeq 0.0042$ at the wall. The grid spacing along x_2 and x_3 is: $\Delta x_t/D \simeq 0.033$ on the axis, $\Delta x_t/D \simeq 0.0261$ at $x_t = \pm D/2$ and $\Delta x_t/D \simeq 0.1251$ at $x_t = \pm 3.5D$ $(t = 2, 3)$.

The inflow is located at $x_1 = 0$ with the following inlet relaxation parameters: $\eta_{3,4,5,6} = -\eta_2 = 1.28$. The target inlet velocity was imposed using the power law profile for turbulent pipe flow (Eq. (100)) with $n = 7.215$ $(U_b/U_{cl} = 0.8247)$. The value of U_b was computed fixing the value of the jet's Reynolds number: $Re_D = \rho U_b D/\mu = 23,000$. Also in this case, a correlated random noise was superimposed to the velocity profile (intensity $0.8\% U_b$) and the imposed inlet temperature was fixed at 300 K.

The four lateral boundaries are non-reflecting outflows with $\sigma = 0.28$ and target pressure equal to 1 atm. The assumed exact transverse terms were set according to the inviscid potential solution for the *axisymmetric stagnation-point flow* [16] with $\beta = 0.18$, the typical outflow Mach number for this flow. The bottom boundary is an adiabatic no-slip wall. Inflow/outflow edge conditions are used on the four top edges and inflow/outflow/outflow corner conditions are used on the relevant four joining corners; outflow/outflow edge conditions are

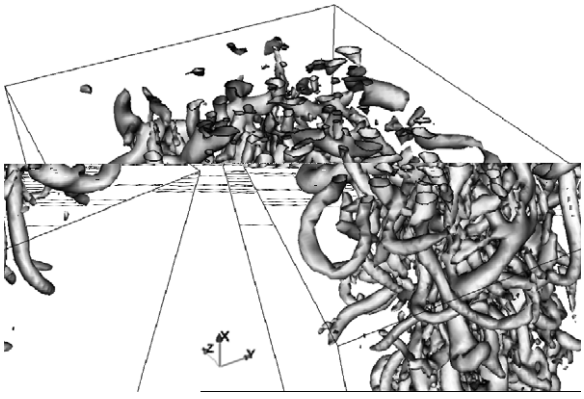

Fig. 20. Free round-jet with 3D-NSCBC: detail of $Q = 0.5$ contours at the boundary.

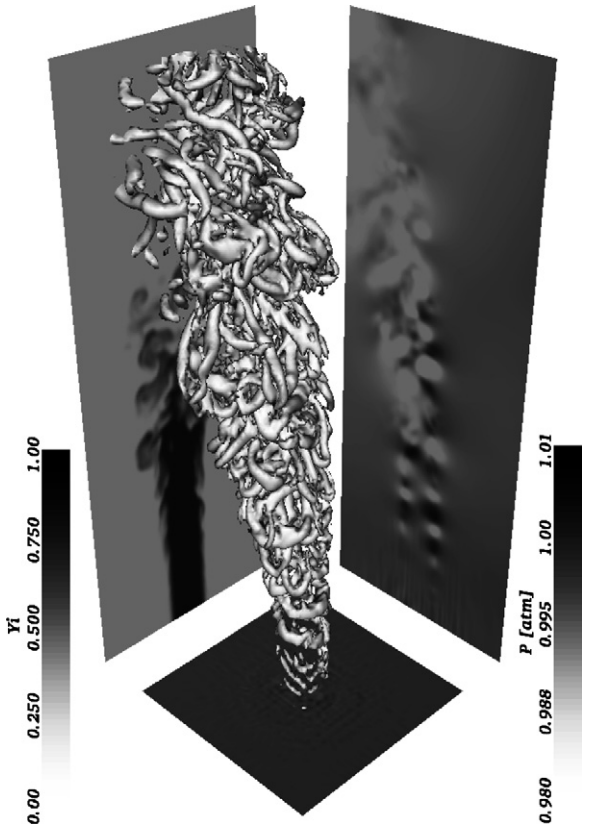

Fig. 21. Free round-jet with standard NSCBC: $Q = 0.5$ contours (center), passive scalar (left) and pressure (right) distributions over orthogonal axial planes ($t = 158.1D/U_b$).

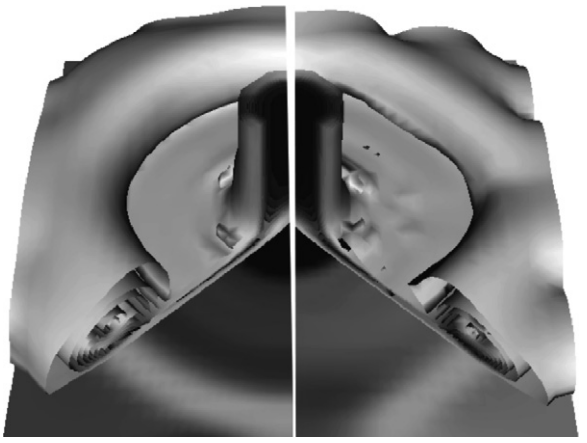

Fig. 22. Impinging round-jet: transverse terms influence on flow distortion. Iso-surfaces of velocity field and wall pressure map in the early stages of the simulation with standard NSCBC boundary conditions (right) and with 3D-NSCBC (left).

used on the four lateral edges, wall/outflow edge conditions are used on the four bottom edges and wall/outflow/outflow corner conditions are used on the four bottom corners (see Fig. 23). The simulation was started from fluid at rest and at reference condition (1 atm, 300 K) all over the domain.

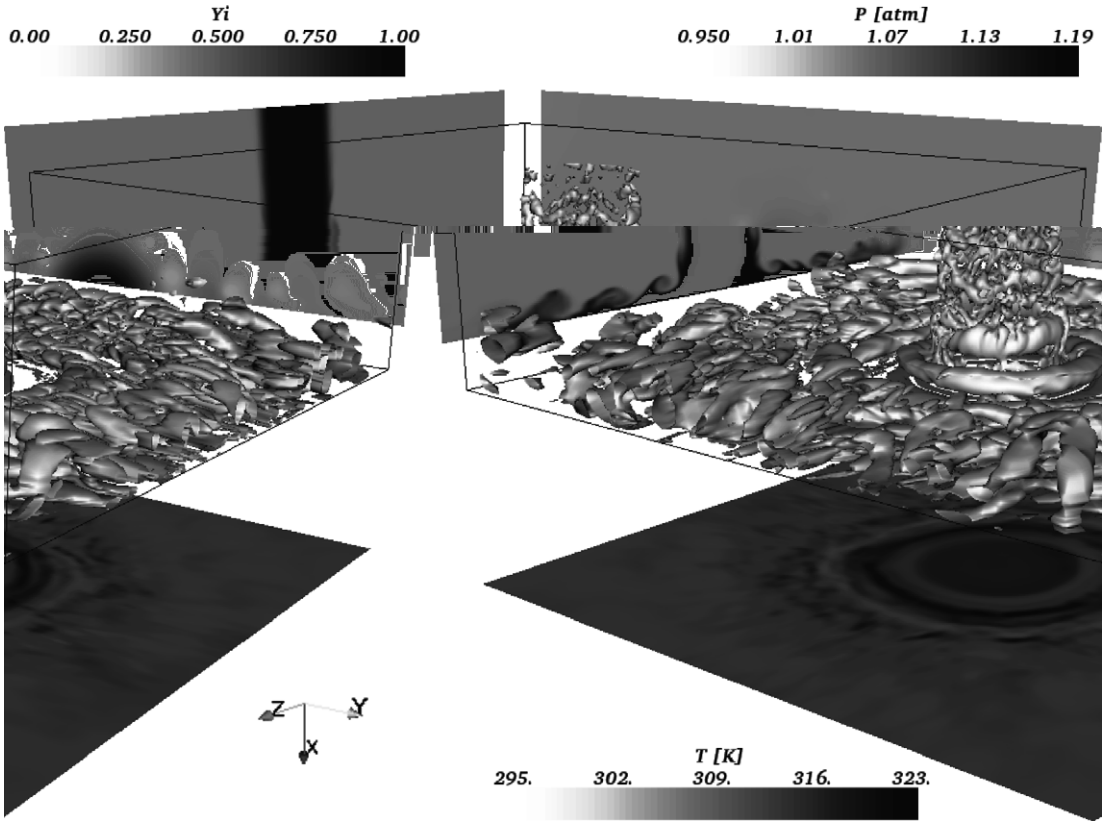

Fig. 23. Impinging round-jet: $Q = 0.5$ contours (center), passive scalar (left) and pressure (right) distributions over orthogonal axial planes and temperature (bottom) distribution over the impingement wall ($t = 52.4D/U_b$).

A preliminary test, made on a quite coarse mesh ($20 \times 42 \times 42$ grid points), is presented in Fig. 22 where the standard NSCBC non-reflecting outflow is compared with the 3D-NSCBC in terms of flow-field distortion. Iso-surfaces of velocity and wall pressure map are shown at the moment the big initial toroidal vortex encounters the domain boundaries. The inclusion of transverse terms allows for a significant reduction in terms of flow distortion and numerical noise; the latter, can be observed as a small perturbation in the vicinity of the impingement zone.

The developed flow field is shown by its coherent vortical structures ($Q = 0.5$ iso-surfaces) in Fig. 23. Pressure and passive scalar distributions over axial planes are projected to the sides and the wall temperature map is shown at the bottom. No significant numerical perturbation is observed on turbulence development, nor in the pressure field; moreover, the wall/outflow compatibility conditions exhibit fairly good robustness and numerical stability.

5. Concluding remarks

A three-dimensional treatment of boundary conditions at edges and corners of fully compressible flow computational domains has been discussed. This very sensitive point of boundary condition was found related to the treatment of convection and pressure gradient developing in the direction parallel to boundary faces, also called transverse terms.

A method involving the inclusion of these transverse effects in the computation of the incoming wave amplitude variations is presented. This method removes the original LODI assumption which is, in general, too stringent to correctly deal with turbulent flows. The work is grounded on the method proposed by Yoo et al. [24] regarding bidimensional flows, which poses additional problems of wave coupling at the edges

and corners of three-dimensional computational domain. A systematic approach to solve edges and corners has been presented and compatibility conditions for inflow/outflow and wall/outflow boundaries discussed. The general methodology to organize the incoming and outcoming waves approximation is based on the NSCBC approach by Poinsot and Lele [12].

The novel technique has shown significant reduction of flow distortion and boundary reflection even when the configuration is characterized by high tridimensionality of the flow field, accompanied by obliquely propagating waves. The obtained 3D-NSCBC non-reflecting outflow, in particular, is characterized by an additional relaxation parameter for transverse terms damping. This poses the problem of specifying a reasonable exact solution for the flow under study. The tests performed have revealed a quite interesting feature on this regard: even when no information is available a priori for the steady solution, transverse relaxation can still be done toward identically zero terms. However, the optimal choice for the transverse relaxation parameter is, in general, related to the typical Mach number for the flow considered.

The proposed solution to the edge/corner wave coupling problem, as well as the compatibility conditions for inflow/outflow and wall/outflow connecting regions, have revealed good numerical stability and low level of spurious boundary reflection for acoustic waves traveling toward the edges and corners of the computational domain, thus allowing high boundary transparency even when computing complex flows.

The 3D-NSCBC method is applicable to compressible turbulent flows in the full subsonic range and is then suitable for a wide range of flow configurations and engineering applications. Furthermore, the method can be readily extended to chemically reacting flows with some additional development.

Acknowledgment

Support was provided by the project NICE (New Integrated Combustion system for Future Passenger Car Engines), TIP3-CT-2004-50620 within the 6th Framework program of the European Union. Computing resources were provided by IDRIS-CNRS (http://www.idris.fr/) and CRIHAN (http://www.crihan.fr/).

Appendix A. The characteristic form of the Navier–Stokes equations

Eqs. (1)–(4) are more conveniently recast in vector form as follows:

$$\frac{\partial \widetilde{\boldsymbol{U}}}{\partial t}+\frac{\partial \widetilde{\boldsymbol{F}}^i}{\partial x_i}+\frac{\partial \widetilde{\boldsymbol{D}}^i}{\partial x_i}=\boldsymbol{0}, \tag{A.1}$$

where $\widetilde{\boldsymbol{U}}=|\rho \quad \rho u_1 \quad \rho u_2 \quad \rho u_3 \quad \rho E \quad \rho Z|^{\mathrm{T}}$ is the vector of conservative variables and $\widetilde{\boldsymbol{F}}^k$ is the flux vector of conservative variables along direction x_k; vectors $\widetilde{\boldsymbol{D}}^k$ represent viscous and diffusive terms only. $\widetilde{\boldsymbol{F}}^k$ and $\widetilde{\boldsymbol{D}}^k$ are explicitly written as follows (δ_{ij} is Kronecker's delta):

$$\widetilde{\boldsymbol{F}}^k=\begin{pmatrix}\rho u_k\\ m_1u_k+\delta_{1k}p\\ m_2u_k+\delta_{2k}p\\ m_3u_k+\delta_{3k}p\\ (\rho E+p)u_k\\ \rho Z u_k\end{pmatrix},\quad \widetilde{\boldsymbol{D}}^k=\begin{pmatrix}0\\ -2\mu A_{1k}\\ -2\mu A_{2k}\\ -2\mu A_{3k}\\ -2\mu u_j A_{kj}+q_k\\ -\rho D\frac{\partial Z}{\partial x_k}\end{pmatrix}, \tag{A.2}$$

the relevant quantities being defined in Section 2.

Let the vector of primitive variables be $\boldsymbol{U}=|\rho \quad u_1 \quad u_2 \quad u_3 \quad p \quad Z|^{\mathrm{T}}$; following the same analysis proposed by Hirsch [5] and Thompson [21,22], Eq. (A.1) is then rewritten in terms of primitive variables as

$$\frac{\partial \boldsymbol{U}}{\partial t}+\boldsymbol{F}^i\frac{\partial \boldsymbol{U}}{\partial x_i}+\boldsymbol{D}=\boldsymbol{0}, \tag{A.3}$$

where $\boldsymbol{D}=\boldsymbol{P}^{-1}\partial\widetilde{\boldsymbol{D}}^i/\partial x_i$ includes all the viscous and diffusive terms and $\boldsymbol{F}^k$ is the non-conservative Jacobian matrix relevant to the kth direction. In the present case

$$\boldsymbol{F}^k = \begin{pmatrix} u_k & \delta_{1k}\rho & \delta_{2k}\rho & \delta_{3k}\rho & 0 & 0 \\ 0 & u_k & 0 & 0 & \delta_{1k}/\rho & 0 \\ 0 & 0 & u_k & 0 & \delta_{2k}/\rho & 0 \\ 0 & 0 & 0 & u_k & \delta_{3k}/\rho & 0 \\ 0 & \delta_{1k}\gamma p & \delta_{2k}\gamma p & \delta_{3k}\gamma p & u_k & 0 \\ 0 & 0 & 0 & 0 & 0 & u_k \end{pmatrix}. \tag{A.4}$$

$\boldsymbol{P} = \partial\widetilde{\boldsymbol{U}}/\partial\boldsymbol{U}$ is the Jacobian matrix to switch between primitive and conservative variables:

$$\boldsymbol{P} = \begin{pmatrix} 1 & 0 & 0 & 0 & 0 & 0 \\ u_1 & \rho & 0 & 0 & 0 & 0 \\ u_2 & 0 & \rho & 0 & 0 & 0 \\ u_3 & 0 & 0 & \rho & 0 & 0 \\ \frac{1}{2}u_k u_k & \rho u_1 & \rho u_2 & \rho u_3 & \frac{1}{\kappa} & 0 \\ Z & 0 & 0 & 0 & 0 & \rho \end{pmatrix}, \tag{A.5}$$

$$\boldsymbol{P}^{-1} = \begin{pmatrix} 1 & 0 & 0 & 0 & 0 & 0 \\ -u_1/\rho & 1/\rho & 0 & 0 & 0 & 0 \\ -u_2/\rho & 0 & 1/\rho & 0 & 0 & 0 \\ -u_3/\rho & 0 & 0 & 1/\rho & 0 & 0 \\ \frac{\kappa}{2}u_k u_k & -\kappa u_1 & -\kappa u_2 & -\kappa u_3 & \kappa & 0 \\ -Z/\rho & 0 & 0 & 0 & 0 & 1/\rho \end{pmatrix} \tag{A.6}$$

with $\kappa = \gamma - 1$.

Each $\boldsymbol{F}^k$ may be diagonalized resorting to the usual transformation:

$$\boldsymbol{S}_k^{-1}\boldsymbol{F}^k\boldsymbol{S}_k = \boldsymbol{\Lambda}^k, \tag{A.7}$$

the eigenvalues being

$$\lambda_1^k = u_k - c, \tag{A.8}$$

$$\lambda_{2,3,4,6}^k = u_k, \tag{A.9}$$

$$\lambda_5^k = u_k + c, \tag{A.10}$$

where c is the speed of sound and

$$\boldsymbol{S}_k = \begin{pmatrix} \frac{1}{2c^2} & \frac{\delta_{1k}}{c^2} & \frac{\delta_{2k}}{c^2} & \frac{\delta_{3k}}{c^2} & \frac{1}{2c^2} & 0 \\ -\frac{\delta_{1k}}{2\rho c} & 1-\delta_{1k} & 0 & 0 & \frac{\delta_{1k}}{2\rho c} & 0 \\ -\frac{\delta_{2k}}{2\rho c} & 0 & 1-\delta_{2k} & 0 & \frac{\delta_{2k}}{2\rho c} & 0 \\ -\frac{\delta_{3k}}{2\rho c} & 0 & 0 & 1-\delta_{3k} & \frac{\delta_{3k}}{2\rho c} & 0 \\ \frac{1}{2} & 0 & 0 & 0 & \frac{1}{2} & 0 \\ 0 & 0 & 0 & 0 & 0 & 1 \end{pmatrix}, \tag{A.11}$$

$$\boldsymbol{S}_k^{-1} = \begin{pmatrix} 0 & -\delta_{1k}\rho c & -\delta_{2k}\rho c & -\delta_{3k}\rho c & 1 & 0 \\ \delta_{1k}c^2 & 1-\delta_{1k} & 0 & 0 & -\delta_{1k} & 0 \\ \delta_{2k}c^2 & 0 & 1-\delta_{2k} & 0 & -\delta_{2k} & 0 \\ \delta_{3k}c^2 & 0 & 0 & 1-\delta_{3k} & -\delta_{3k} & 0 \\ 0 & \delta_{1k}\rho c & \delta_{2k}\rho c & \delta_{3k}\rho c & 1 & 0 \\ 0 & 0 & 0 & 0 & 0 & 1 \end{pmatrix}. \tag{A.12}$$

Depending on the type of boundary condition considered (face/edge/corner), a different number of characteristic directions should be taken into account (one/two/three) simultaneously: the three cases are summarized in the following sections.

A.1. Characteristic formulation along one direction for faces

Supposing that the boundary is orthogonal to the x_1 direction, the characteristic waves considered will be those traveling along x_1; therefore, only $\boldsymbol{F}^1$ needs to be diagonalized and Eq. (A.3) can be then written as

$$\frac{\partial \boldsymbol{U}}{\partial t} + \boldsymbol{S}_1 \boldsymbol{\Lambda}^1 \boldsymbol{S}_1^{-1} \frac{\partial \boldsymbol{U}}{\partial x_1} + \boldsymbol{F}^2 \frac{\partial \boldsymbol{U}}{\partial x_2} + \boldsymbol{F}^3 \frac{\partial \boldsymbol{U}}{\partial x_3} + \boldsymbol{D} = \boldsymbol{0}. \tag{A.13}$$

The eigenvalues (i.e. the propagation velocities of the characteristic waves) are

$$\lambda_1 = u_1 - c, \quad \lambda_{2,3,4,6} = u_1, \quad \lambda_5 = u_1 + c. \tag{A.14}$$

Following the procedure proposed by Thompson [21], a vector $\boldsymbol{\mathcal{L}}$ may be conveniently defined as

$$\boldsymbol{\mathcal{L}} = \boldsymbol{\Lambda}^1 \boldsymbol{S}_1^{-1} \frac{\partial \boldsymbol{U}}{\partial x_1}, \tag{A.15}$$

whose components $\mathcal{L}_i$ are the amplitude time variations of the characteristic waves [12]:

$$\boldsymbol{\mathcal{L}} = \begin{pmatrix} \lambda_1 \left(\frac{\partial p}{\partial x_1} - \rho c \frac{\partial u_1}{\partial x_1} \right) \\ \lambda_2 \left(c^2 \frac{\partial \rho}{\partial x_1} - \frac{\partial p}{\partial x_1} \right) \\ \lambda_3 \frac{\partial u_2}{\partial x_1} \\ \lambda_4 \frac{\partial u_3}{\partial x_1} \\ \lambda_5 \left(\frac{\partial p}{\partial x_1} + \rho c \frac{\partial u_1}{\partial x_1} \right) \\ \lambda_6 \frac{\partial Z}{\partial x_1} \end{pmatrix}. \tag{A.16}$$

Eq. (A.13) is finally rewritten as a function of the wave amplitude variations and the relevant formulation in terms of conservative variables can be obtained pre-multiplying by $\boldsymbol{P}$:

$$\frac{\partial \boldsymbol{U}}{\partial t} + \boldsymbol{d} + \boldsymbol{F}^2 \frac{\partial \boldsymbol{U}}{\partial x_2} + \boldsymbol{F}^3 \frac{\partial \boldsymbol{U}}{\partial x_3} + \boldsymbol{D} = \boldsymbol{0}, \tag{A.17}$$

$$\frac{\partial \widetilde{\boldsymbol{U}}}{\partial t} + \boldsymbol{P}\boldsymbol{d} + \frac{\partial \widetilde{\boldsymbol{F}}^2}{\partial x_2} + \frac{\partial \widetilde{\boldsymbol{F}}^3}{\partial x_3} + \frac{\partial \widetilde{\boldsymbol{D}}^i}{\partial x_i} = \boldsymbol{0}, \tag{A.18}$$

where

$$\boldsymbol{d} = \boldsymbol{S}_1 \boldsymbol{\mathcal{L}} = \begin{pmatrix} \frac{1}{c^2} \left[\mathcal{L}_2 + \frac{1}{2} (\mathcal{L}_5 + \mathcal{L}_1) \right] \\ \frac{1}{2\rho c} (\mathcal{L}_5 - \mathcal{L}_1) \\ \mathcal{L}_3 \\ \mathcal{L}_4 \\ \frac{1}{2} (\mathcal{L}_5 + \mathcal{L}_1) \\ \mathcal{L}_6 \end{pmatrix}. \tag{A.19}$$

It should be noted that Eq. (A.17) without transverse derivatives and diffusive terms constitutes the so-called LODI system of the standard NSCBC approach [12]:

$$
\begin{cases}
\frac{\partial \rho}{\partial t} + \frac{1}{c^2}\left[\mathcal{L}_2 + \frac{1}{2}(\mathcal{L}_5 + \mathcal{L}_1)\right] = 0, \\
\frac{\partial u_1}{\partial t} + \frac{1}{2\rho c}(\mathcal{L}_5 - \mathcal{L}_1) = 0, \\
\frac{\partial u_2}{\partial t} + \mathcal{L}_3 = 0, \\
\frac{\partial u_3}{\partial t} + \mathcal{L}_4 = 0, \\
\frac{\partial p}{\partial t} + \frac{1}{2}(\mathcal{L}_5 + \mathcal{L}_1) = 0, \\
\frac{\partial Z}{\partial t} + \mathcal{L}_6 = 0.
\end{cases}
\tag{A.20}
$$

A.3. Characteristic formulation along three directions for corners

Characteristic waves are considered in all the three directions; all the flux matrix are diagonalized and Eq. (A.3) becomes

$$\frac{\partial \boldsymbol{U}}{\partial t} + \boldsymbol{S}_1 \boldsymbol{\Lambda} \boldsymbol{S}_1^{-1} \frac{\partial \boldsymbol{U}}{\partial x_1} + \boldsymbol{S}_2 \boldsymbol{M} \boldsymbol{S}_2^{-1} \frac{\partial \boldsymbol{U}}{\partial x_2} + \boldsymbol{S}_3 \boldsymbol{N} \boldsymbol{S}_3^{-1} \frac{\partial \boldsymbol{U}}{\partial x_3} + \boldsymbol{D} = \boldsymbol{0}. \tag{A.30}$$

The eigenvalues of $\boldsymbol{F}^1$, $\boldsymbol{F}^2$ and $\boldsymbol{F}^3$ are λ_i, μ_i and v_i, respectively:

$$\lambda_1 = u_1 - c, \quad \lambda_{2,3,4,6} = u_1, \quad \lambda_5 = u_1 + c, \tag{A.31}$$

$$\mu_1 = u_2 - c, \quad \mu_{2,3,4,6} = u_2, \quad \mu_5 = u_2 + c, \tag{A.32}$$

$$v_1 = u_3 - c, \quad v_{2,3,4,6} = u_3, \quad v_5 = u_3 + c. \tag{A.33}$$

Wave amplitude time variations are defined as

$$\boldsymbol{\mathcal{L}} = \boldsymbol{\Lambda} \boldsymbol{S}_1^{-1} \frac{\partial \boldsymbol{U}}{\partial x_1}, \tag{A.34}$$

$$\boldsymbol{\mathcal{M}} = \boldsymbol{M} \boldsymbol{S}_2^{-1} \frac{\partial \boldsymbol{U}}{\partial x_2}, \tag{A.35}$$

$$\boldsymbol{\mathcal{N}} = \boldsymbol{N} \boldsymbol{S}_3^{-1} \frac{\partial \boldsymbol{U}}{\partial x_3}, \tag{A.36}$$

where $\boldsymbol{\mathcal{L}}$ and $\boldsymbol{\mathcal{M}}$ are expressed by Eqs. (A.16) and (A.26), respectively and $\boldsymbol{\mathcal{N}}$ is

$$\boldsymbol{\mathcal{N}} = \begin{pmatrix} v_1 \left(\frac{\partial p}{\partial x_3} - \rho c \frac{\partial u_3}{\partial x_3} \right) \\ v_2 \frac{\partial u_1}{\partial x_3} \\ v_3 \frac{\partial u_2}{\partial x_3} \\ v_4 \left(c^2 \frac{\partial \rho}{\partial x_3} - \frac{\partial p}{\partial x_3} \right) \\ v_5 \left(\frac{\partial p}{\partial x_3} + \rho c \frac{\partial u_3}{\partial x_3} \right) \\ v_6 \frac{\partial Z}{\partial x_3} \end{pmatrix}. \tag{A.37}$$

Conservation laws in terms of primitive and conservative variables are respectively:

$$\frac{\partial \boldsymbol{U}}{\partial t} + \boldsymbol{d} + \boldsymbol{e} + \boldsymbol{f} + \boldsymbol{D} = \boldsymbol{0}, \tag{A.38}$$

$$\frac{\partial \widetilde{\boldsymbol{U}}}{\partial t} + \boldsymbol{P}\boldsymbol{d} + \boldsymbol{P}\boldsymbol{e} + \boldsymbol{P}\boldsymbol{f} + \frac{\partial \widetilde{\boldsymbol{D}}^i}{\partial x_i} = \boldsymbol{0}, \tag{A.39}$$

where $\boldsymbol{d}$ is expressed by Eq. (A.19), $\boldsymbol{e}$ is expressed by Eq. (A.29) and $\boldsymbol{f}$ is

$$\boldsymbol{f} = \boldsymbol{S}_3 \boldsymbol{\mathcal{N}} = \begin{pmatrix} \frac{1}{c^2} \left[\mathcal{N}_4 + \frac{1}{2} (\mathcal{N}_5 + \mathcal{N}_1) \right] \\ \mathcal{N}_2 \\ \mathcal{N}_3 \\ \frac{1}{2\rho c} (\mathcal{N}_5 - \mathcal{N}_1) \\ \frac{1}{2} (\mathcal{N}_5 + \mathcal{N}_1) \\ \mathcal{N}_6 \end{pmatrix}. \tag{A.40}$$

Appendix B. Computing the transverse terms from conservative variables' fluxes

When the solver integrates the Navier–Stokes equations written in conservative form, it may be more convenient to directly relate the transverse terms vector $\boldsymbol{\mathcal{T}}$ to the flux vector $\widetilde{\boldsymbol{F}}^k$. Considering, for instance, a face boundary orthogonal to x_1, Eq. (13) in vector form reads

$$\frac{\partial \boldsymbol{U}}{\partial t} + \boldsymbol{d} - \boldsymbol{\mathcal{T}} = \boldsymbol{0}, \tag{B.1}$$

where $-\boldsymbol{\mathcal{T}}$ represents the transverse fluxes and pressure gradients along x_2 and x_3:

$$\boldsymbol{\mathcal{T}} = -\boldsymbol{F}^t \frac{\partial \boldsymbol{U}}{\partial x_t} \quad (t = 2, 3). \tag{B.2}$$

By definition, the non-conservative Jacobian matrix $\boldsymbol{F}^k$ is related to the flux vector $\widetilde{\boldsymbol{F}}^k$ by the following relation:

$$\boldsymbol{P}\boldsymbol{F}^k \frac{\partial \boldsymbol{U}}{\partial x_k} = \frac{\partial \widetilde{\boldsymbol{F}}^k}{\partial x_k}. \tag{B.3}$$

Pre-multiplying the above equation by $\boldsymbol{P}^{-1}$, the expression for $\boldsymbol{\mathcal{T}}$ then becomes

$$\boldsymbol{\mathcal{T}} = -\boldsymbol{P}^{-1} \frac{\partial \widetilde{\boldsymbol{F}}^t}{\partial x_t} \quad (t = 2, 3) \tag{B.4}$$

with components

$$\mathcal{T}_1 = -\frac{\partial F_1^t}{\partial x_t}, \tag{B.5}$$

$$\mathcal{T}_2 = -\frac{1}{\rho}\left(\frac{\partial F_2^t}{\partial x_t} - u_1 \frac{\partial F_1^t}{\partial x_t}\right), \tag{B.6}$$

$$\mathcal{T}_3 = -\frac{1}{\rho}\left(\frac{\partial F_3^t}{\partial x_t} - u_2 \frac{\partial F_1^t}{\partial x_t}\right), \tag{B.7}$$

$$\mathcal{T}_4 = -\frac{1}{\rho}\left(\frac{\partial F_4^t}{\partial x_t} - u_3 \frac{\partial F_1^t}{\partial x_t}\right), \tag{B.8}$$

$$\mathcal{T}_5 = -(\gamma - 1)\left(\frac{\partial F_5^t}{\partial x_t} + \frac{u_k u_k}{2}\frac{\partial F_1^t}{\partial x_t} - u_k \frac{\partial F_{k+1}^t}{\partial x_t}\right), \tag{B.9}$$

$$\mathcal{T}_6 = -\frac{1}{\rho}\left(\frac{\partial F_6^t}{\partial x_t} - Z \frac{\partial F_1^t}{\partial x_t}\right). \tag{B.10}$$

The same relations for an edge boundary can be easily obtained by considering that, in that case, the vector $\boldsymbol{\mathcal{T}}$ represents fluxes and pressure gradients along the edge direction only.

References

[1] M. Baum, T. Poinsot, D. Thévenin, Accurate boundary conditions for multicomponent reactive flows, Journal of Computational Physics 116 (2) (1995) 247–261.
[2] C. Bogey, C. Bailly, An analysis of the corrections between the turbulent flow and the sound pressure fields of subsonic jets, Journal of Fluid Mechanics 583 (2007) 71–97.
[3] T. Colonius, S. Lele, P. Moin, The free compressible viscous vortex, Journal of Fluid Mechanics 230 (1991) 45–73.
[4] F. Ducros, F. Laporte, T. Soulères, V. Guinot, P. Moinat, B. Caruelle, High-order fluxes for conservative skew-symmetric-like schemes in structured meshes: application to compressible flows, Journal of Computational Physics 161 (2000) 114–139.
[5] C. Hirsch, Numerical Computation of Internal and External Flows, vol. 2, John Wiley & Sons Ltd., 1990.
[6] R. Hixon, S. Shih, R. Mankabadi, Evaluation of boundary conditions for computational aeroacoustics, AIAA Journal 33 (11) (1995) 2006–2012.
[7] G. Jiang, C. Shu, Efficient implementation of weighted ENO schemes, Journal of Computational Physics 126 (1996) 202–228.
[8] M. Klein, A. Sadiki, J. Janicka, A digital filter based generation of inflow data for spatially developing direct numerical or large eddy simulations, Journal of Computational Physics 186 (2003) 652–665.

[9] F. Nicoud, Defining wave amplitude in characteristic boundary conditions, Journal of Computational Physics 149 (1999) 418–422.
[10] F. Nicoud, F. Ducros, Subgrid-scale stress modelling based on the square of the velocity gradient tensor, Flow, Turbulence and Combustion 62 (3) (1999) 183–200.
[11] N. Okong'o, J. Bellan, Consistent boundary conditions for multicomponent real gas mixtures based on characteristic waves, Journal of Computational Physics 176 (2) (2002) 330–344.
[12] T. Poinsot, S. Lele, Boundary conditions for direct simulations of compressible viscous flows, Journal of Computational Physics 101 (1992) 104–129.
[13] W. Polifke, C. Wall, P. Moin, Partially reflecting and non-reflecting boundary conditions for simulation of compressible viscous flow, Journal of Computational Physics 213 (1) (2006) 437–449.
[14] R. Prosser, Improved boundary conditions for the direct numerical simulation of turbulent subsonic flows. I. Inviscid flows, Journal of Computational Physics 207 (2005) 736–768.
[15] D. Rudy, J. Strikwerda, A nonreflecting outflow boundary condition for subsonic Navier–Stokes calculations, Journal of Computational Physics 36 (1980) 55–70.
[16] H. Schlichting, K. Gersten, Boundary-Layer Theory, eighth ed., Springer-Verlag, Berlin, Heidelberg, 2000.
[17] J. Sutherland, C. Kennedy, Improved boundary conditions for viscous, reacting, compressible flows, Journal of Computational Physics 191 (2) (2003) 502–524.
[18] R. Swanson, E. Turkel, On central-difference and upwind schemes, Journal of Computational Physics 101 (1992) 292–306.
[19] C. Tam, Advances in numerical boundary conditions for computational aeroacoustics, Journal of Computational Acoustics 6 (4) (1998) 377–402.
[20] S. Tatsumi, L. Martinelli, A. Jameson, Flux-limited schemes for the compressible Navier–Stokes equations, AIAA Journal 33 (2) (1995) 252–261.
[21] K.W. Thompson, Time dependent boundary conditions for hyperbolic systems, Journal of Computational Physics 68 (1987) 1–24.
[22] K.W. Thompson, Time dependent boundary conditions for hyperbolic systems: II, Journal of Computational Physics 89 (1990) 439–461.
[23] M. Valorani, B. Favini, On the numerical integration of multi-dimensional, initial boundary value problems for the Euler equations in quasi-linear form, Numerical Methods for Partial Differential Equations 14 (6) (1998) 781–814.
[24] C. Yoo, Y. Wang, A. Trouvé, H. Im, Characteristic boundary conditions for direct simulations of turbulent counterflow flames, Combustion Theory and Modeling 9 (4) (2005) 617–646.